

An Infrared Spectroscopic Sequence of M, L and T Dwarfs¹

Michael C. Cushing^{2,3}

SETI Institute, MS 245-3 NASA Ames Research Center, Moffett Field, CA 94035

`mcushing@mail.arc.nasa.gov`

John T. Rayner

Institute for Astronomy, University of Hawai'i, 2680 Woodlawn Drive, Honolulu, HI 96822

`rayner@ifa.hawaii.edu`

and

William D. Vacca²

SOFIA-USRA, NASA Ames Research Center MS 144-2, Moffett Field, CA 94035

`wvacca@mail.arc.nasa.gov`

ABSTRACT

We present a 0.6–4.1 μm spectroscopic sequence of M, L, and T dwarfs. The spectra have $R \equiv \lambda/\Delta\lambda \approx 2000$ from 0.9 to 2.4 μm and $R=2500-200$ from 2.9 to 4.1 μm . These new data nearly double the number of L and T dwarfs that have reported *L*-band spectra. The near-infrared spectra are combined with previously published red-optical spectra to extend the wavelength coverage to $\sim 0.6 \mu\text{m}$. Prominent atomic and molecular absorption features are identified including neutral lines of Al, Fe, Mg, Ca, Ti, Na, and K and 19 new weak CH_4 absorption features in the *H*-band spectra of mid- to late-type T dwarfs. In addition, we detect for the first time the 0–0 band of the $A \ ^4\Pi - X \ ^4\Sigma^-$ transition of VO at $\sim 1.06 \mu\text{m}$ in the spectra of L dwarfs and the P and R branches of the ν_3 band of CH_4 in the spectrum of a T dwarf. The equivalent widths of the refractory atomic features all decrease with increasing spectral type and are absent by a spectral type of $\sim \text{L0}$, except for the 1.189 μm Fe I line which persists to

¹Based in part on data collected at Subaru Telescope, which is operated by the National Astronomical Observatory of Japan.

²Visiting Astronomer at the Infrared Telescope Facility, which is operated by the University of Hawai'i under cooperative Agreement no. NCC 5-538 with the National Aeronautics and Space Administration, Office of Space Science, Planetary Astronomy Program.

³Spitzer Fellow

at least \sim L3. We compute the bolometric luminosities of the dwarfs in our sample with measured parallaxes and find good agreement with previously published results that use L' -band photometry to account for the flux emitted from 2.5 to 3.6 μm . Finally, 2MASS J2224381–0158521 (L4.5) has an anomalously red spectrum and the strongest $\Delta\nu=+2$ CO bands in our sample. This may be indicative of unusually thick condensate clouds and/or low surface gravity.

Subject headings: infrared: stars — stars: late-type — stars: low-mass, brown dwarfs — stars: fundamental parameters — stars:individual (2MASS J2224381–0158521)

1. Introduction

Since the discovery of the first bona fide brown dwarfs (BDs) (Basri et al. 1996; Rebolo et al. 1996; Nakajima et al. 1995), hundreds of very low-mass stars and BDs, collectively known as ultracool dwarfs, have been discovered in wide-field surveys such as the 2 Micron All Sky Survey (2MASS; Skrutskie et al. 1997), the Deep Near Infrared Southern Sky Survey (DENIS; Epchtein et al. 1997), and the Sloan Digital Sky Survey (SDSS; York et al. 2000). The spectra of many of these ultracool dwarfs were sufficiently distinct from those of the latest M dwarfs that the creation of two new spectral types, ‘L’ (Kirkpatrick et al. 1999; Martín et al. 1999) and ‘T’ (Burgasser 2001; Burgasser et al. 2002a), was warranted. The spectra of L dwarfs exhibit weak oxide bands (TiO and VO), strong hydride bands (FeH and CrH), and alkali lines (Na, K, Rb, and Cs) in the red optical and H₂O, FeH, and CO absorption bands in the near-infrared. The spectra of T dwarfs also show absorption due to alkali lines in the optical (although the Na and K lines are highly pressure-broadened) but, in contrast to the L dwarfs, exhibit strong CH₄ bands along with H₂O bands and collision-induced absorption (CIA) due to H₂ in the near-infrared.

Since the spectral energy distributions of ultracool dwarfs peak in the near-infrared, it is advantageous to study them at these wavelengths. There have been numerous near-infrared spectroscopic studies of M, L, and T dwarfs (e.g., Jones et al. 1994; Ali et al. 1995; Leggett et al. 1996; Reid et al. 2001; Leggett et al. 2001; Burgasser et al. 2000, 2002a) but the majority of the published spectra have low spectral resolving powers ($R \equiv \lambda/\Delta\lambda \lesssim 500$) and a range of signal-to-noise ratios (S/N). Although such spectra are suitable for studying variations in gross spectral morphology (e.g. defining spectral classification schemes, Reid et al. 2001; Geballe et al. 2002; Burgasser et al. 2002a), higher resolution spectra are required for more detailed analyses. For example, Saumon et al. (2000) analyzed an $R=3000$ spectrum of Gl 229B (T6.5) to constrain its metallicity while Cushing et al. (2003) identified nearly 100 new weak FeH absorption features in $R\approx 2000$ spectra of late-type M dwarfs and L dwarfs. McLean et al. (2003) have recently published a large sample of high quality, moderate resolution ($R=2000$), near-infrared ($\sim 1\text{--}2.3 \mu\text{m}$) spectra of late-type M, L, and T dwarfs, which greatly enhances the quality and number of ultracool dwarf spectra available for such analyses.

In contrast to the large number of published spectra covering from 1 to 2.5 μm , relatively little spectroscopic work on M, L, and T dwarfs has been done at $\lambda > 2.5\mu\text{m}$, primarily due to the difficulty of observing from the ground at these wavelengths. Berriman & Reid (1987) were the first to detect H₂O absorption at $\sim 3\ \mu\text{m}$ in very low resolution ($R \approx 70$) spectra of early- to mid-type M dwarfs. Jones et al. (1995) and Jones et al. (2002) used moderate resolution spectra obtained from the ground and space to study this H₂O band in a small sample of M dwarf spectra. Even fewer spectra of L and T dwarfs at $\lambda > 2.5\ \mu\text{m}$ have been published. The ν_3 fundamental band of CH₄ at $\sim 3.3\ \mu\text{m}$ has been detected in the low resolution spectra of two L dwarfs (Noll et al. 2000) and two T dwarfs (Oppenheimer et al. 1998; Burgasser 2001) while the fundamental CO band at 4.7 μm has been detected in the spectrum of Gl 229B (Noll et al. 1997). Recent observations from the *Spitzer Space Telescope* (Roellig et al. 2004) have also revealed H₂O, CH₄, and NH₃ absorption in the mid-infrared spectra of an L dwarf and a T dwarf. The paucity of M, L, and T dwarf spectra at these wavelengths is unfortunate since the H₂O, CH₄, CO, and NH₃ bands are useful probes of the atmospheric physics and chemistry of ultracool dwarfs (Saumon et al. 2003a,b).

We have therefore undertaken a spectroscopic survey of M, L, and T dwarfs with the goal of creating a sample of high S/N (>50), moderate resolution ($R \approx 2000$) spectra covering a broad wavelength range (~ 0.9 to 4.1 μm). We present the first results of this survey in this paper. In §2 we discuss the observations and data reduction. We describe the identification of prominent atomic and molecular absorption features as well as quantify the changes in the strengths of these features with spectral type in §3. In §4, we discuss two objects of interest; 2MASS 2224–0158 (L4.5), which exhibits an anomalously red near-infrared spectrum with deep CO bands and DENIS 0255–4700, a late-type L dwarf (L8) that exhibits CH₄ absorption in both the *H* and *K* bands. In §5 we compute the bolometric luminosities of the ultracool dwarfs in our sample and finally in §6 we present a summary of our results.

2. Observations and Data Reduction

Our sample consists of 11 M dwarfs, 13 L dwarfs, and 2 T dwarfs. Table 1 lists the dwarfs’ designations, spectral types, *J*-, *H*-, *K*-, and *L*’-band magnitudes, and parallaxes. Eight of the M dwarfs were selected from the list of primary spectral standards of Kirkpatrick et al. (1991); we have augmented this list with Gl 388 (AD Leo), LP 944–20, and BRI 0021–0214. The M dwarf spectral types are based on optical spectroscopy and are from Kirkpatrick et al. (1991, 1995, 1999). The L and T dwarfs were drawn from the discoveries in 2MASS (Kirkpatrick et al. 1999, 2000; Reid et al. 2000; Gizis et al. 2000; Burgasser et al. 2000; Wilson et al. 2003), DENIS (Martín et al. 1999), and SDSS (Leggett et al. 2000; Fan et al. 2000). We also included Kelu–1 which was discovered in a proper-motion survey (Ruiz et al. 1997). The L dwarf spectral types are based on optical spectroscopy and are from the L dwarf database maintained by J. D. Kirkpatrick¹. The T dwarf

¹http://spider.ipac.caltech.edu/staff/davy/ARCHIVE/index_L_spec.html

spectral types are based on near-infrared spectroscopy and are from Burgasser et al. (2002a).

We obtained near-infrared spectra of the 26 dwarfs listed in Table 1 using two instruments: SpeX (Rayner et al. 2003), mounted on the 3.0 m NASA Infrared Telescope Facility (IRTF), and the Infrared Camera and Spectrograph (IRCS, Kobayashi et al. 2000), mounted on the 8.2 m Subaru telescope. SpeX was used for the majority of the observations while the IRCS was used to obtain *L*-band spectra for the faintest targets. The following three sub-sections describe the acquisition and reduction of the data, the absolute flux calibration of the spectra, and the merging of the SpeX, IRCS, and published red-optical spectra to produce absolutely flux-calibrated 0.6–4.1 μm spectra.

2.1. SpeX Observations

SpeX is a 0.8–5.5 μm , medium-resolution, cross-dispersed spectrograph equipped with a 1024×1024 Aladdin 3 InSb array (Rayner et al. 2003). The entire 0.8 to 5.5 μm wavelength range can be covered at $R \approx 2000$ with two cross-dispersed modes. The SXD mode provides simultaneous coverage of the 0.8–2.4 μm wavelength range, except for a 0.6 μm gap between the *H* and *K* bands, while the LXD1.9, LXD2.1, and LXD2.3 modes cover the 1.9–4.2, 2.1–5.0 and 2.3–5.5 μm wavelength ranges, respectively. The length of the slit in all of these modes is 15".

The observations were conducted over a period of three years beginning with SpeX commissioning in 2000 May and ending in 2003 October. A log of the observations, including the UT date of observation, spectroscopic mode, resolving power, total on-source integration time, and associated telluric standard star, is given in Table 2. The 0".3 and 0".5 slits were used in the SXD mode and provide a resolving power of 2000 and 1200, respectively. Three slits with widths of 0".3, 0".5, and 0".8, corresponding to a resolving power of 2500, 1515, and 938, respectively, were used in the LXD modes.

To facilitate subtraction of the additive components of the total signal (electronic bias level, dark current, sky and background emission), the observations were obtained in a series of exposures in which the target was placed at two different positions along the slit separated by 7".8. An A0 V star was observed before or after each target to correct for absorption due to the Earth’s atmosphere and to flux calibrate the science object spectra. The airmass difference between the object and “telluric standard” was almost always less than 0.1 and usually less than 0.05. However, in a few cases where there was a paucity of nearby A0 V stars, the airmass difference was as large as 0.2. Finally, a set of flat field exposures and argon arc lamp exposures was taken after each object/standard pair for flat fielding and wavelength calibration purposes.

We reduced the data using Spextool (Cushing et al. 2004), the facility IDL-based data reduction package for SpeX. The initial image processing consisted of correcting each science frame for non-linearity, subtracting the pairs of images taken at the two different slit positions and dividing the pair-subtracted images by a normalized flat field. The spectra were then optimally extracted and wavelength calibrated. All wavelengths are given in vacuum. The dwarf spectra were corrected

for telluric absorption and flux calibrated (to $\pm \sim 10\%$) using the extracted A0 V spectra and the technique described by Vacca et al. (2003). For each cross-dispersed mode, the spectra from different orders were merged together to form a continuous spectrum. In principle, the flux density levels of the spectra in two overlapping orders should match exactly but in practice we find mismatches of up to 3% but typically less than 1%. Any mismatch was removed by scaling one spectrum to the level of the other. The combined spectra were then smoothed with a Savitzky-Golay kernel (Press et al. 1992) whose width was 1.5 times the slit width measured in pixels. Each LX D spectrum was scaled to match the flux density level of the corresponding SX D spectrum and then the two spectra were combined.

Although the spectra in adjacent orders are scaled to a common flux density level during the merging process, errors can be introduced in the relative flux density levels of the spectra if the S/N in the overlap regions, which is used to determine the scaling factor, is low. Such is the case for dwarf stars with spectral types \gtrsim M6 because of the strong intrinsic water absorption bands present at the wavelengths of the order overlaps. Therefore we computed synthetic $J - H$, $H - K$, and $K - L'$ colors of the dwarfs from our sample and compared them with the colors derived from the published photometry presented in Table 1 to determine if any errors were introduced during the merging process.

The synthetic color for two bandpasses X and Y is given by,

$$X - Y = -2.5 \times \log \left[\frac{\int \lambda f_{\lambda}^{\text{obj}}(\lambda) T_X(\lambda) d\lambda}{\int \lambda f_{\lambda}^{\text{Vega}}(\lambda) T_X(\lambda) d\lambda} \right] + 2.5 \times \log \left[\frac{\int \lambda f_{\lambda}^{\text{obj}}(\lambda) T_Y(\lambda) d\lambda}{\int \lambda f_{\lambda}^{\text{Vega}}(\lambda) T_Y(\lambda) d\lambda} \right] \quad (1)$$

where $f_{\lambda}^{\text{Vega}}(\lambda)$ is the flux density of Vega, $f_{\lambda}^{\text{obj}}(\lambda)$ is the flux density of the object, and $T(\lambda)$ is the transmission function for each bandpass, which we assume to be given by the product of the filter transmission and the typical atmospheric transmission at an airmass of 1 for the site at which the observation was conducted. For $f_{\lambda}^{\text{Vega}}(\lambda)$ we used a Kurucz model of Vega ($T_{\text{eff}} = 9550$ K, $\log g = 3.950$, $v_{\text{rot}} = 25$ km s $^{-1}$, and $v_{\text{turb}} = 2$ km s $^{-1}$), scaled to the flux density at $\lambda=5556$ Å given by Mégessier (1995). Equation 1 assumes that Vega has a color of zero. The factors of λ inside the integrals convert the energy flux densities f_{λ} to photon flux densities, which ensures that the integrated fluxes are proportional to the observed photon count-rate (e.g., Koornneef et al. 1986; Buser & Kurucz 1992). The CIT JHK , and MKO L' transmission functions were kindly provided by S. Leggett (2002 & 2003, private communication) while the 2MASS filter transmissions are from Cohen et al. (2003)². We computed the residuals ($\delta_{X-Y} = (X - Y)_{\text{obs}} - (X - Y)_{\text{synth}}$) between the observed and synthetic $J - H$, $H - K$, and $K - L'$ colors of each dwarf. The average residuals are given in Table 3 and indicate that no significant errors were introduced in the relative flux density levels of spectra in adjacent orders during the order merging process.

²Note that the λ factors should be removed from Equation 1 when using the 2MASS filter transmission curves from Cohen et al. (2003) because the curves have already been multiplied by λ .

The final step in the reduction process was to absolutely flux calibrate the spectra using the published photometry listed in Table 1. For each spectrum, we computed correction factors given by,

$$C_X = 10^{-0.4m_X} \times \frac{\int \lambda f_\lambda^{\text{Vega}}(\lambda) T_X(\lambda) d\lambda}{\int \lambda f_\lambda^{\text{obs}}(\lambda) T_X(\lambda) d\lambda} \quad (2)$$

where m_X is the magnitude of the object in the J , H , and K bands and the remaining variables have the same meaning as in Equation 1. The errors in the correction factors were computed using the errors in the published magnitudes. Each spectrum was then multiplied by the weighted average of the J -, H - and K -band correction factors. The average correction factors ranged from 0.9 to 1.05 with a median value of 0.92.

2.2. IRCS Observations

The IRCS is a facility infrared imager and spectrograph for the 8.2m Subaru telescope. The imager, which is equipped with a 1024×1024 Alladin 3 InSb array, also contains grisms for low-resolution spectroscopy. We used the L -band grism (2.90–4.16 μm) with slit widths of $0''.3$ and $0''.6$ to achieve spectral resolving powers of ~ 425 and ~ 212 , respectively.

A log of the observations, including the UT date of observation, the resolving power R , total on-source integration time and A0 V telluric standard star, is given in Table 4. The observing strategy was identical to that employed in the SpeX observations. A series of exposures were taken in pairs with the targets at two different positions separated by $5''$ along the $20''$ -long slit. A nearby A0 V star was also observed for each science object to correct for absorption due to the Earth’s atmosphere and a series of flat field exposures and dark frames was taken at the end of each night.

The spectra were extracted using a modified version of Spextool (Cushing et al. 2004). Each pair of target exposures was subtracted and then flat fielded. The spectra were then extracted and wavelength calibrated using sky emission features. The telluric correction process is much simpler than in the case of the SpeX observations because at these wavelengths, the continuum of the A0 V standard star is well approximated by a blackbody and the hydrogen lines are relatively weak. Therefore, we divided the object spectrum by the standard star spectrum to remove the telluric absorption and instrument throughput and then multiplied the result by a Planck function of 9500 K, the effective temperature of A0 V stars (Tokunaga 2000), to restore the continuum shape of the object.

The IRCS spectra must be absolutely flux calibrated using L' -band photometry before they can be combined with the SpeX spectra since the two sets of spectra do not overlap in wavelength. DENIS 0255–4700 lacks a published L' magnitude so we observed it at L' using the SpeX guider camera on 2003 October 03 UT and measured $m_{L'} = 10.2 \pm 0.1$. After the IRCS spectra are flux calibrated using the L' -band photometry they were merged with the SpeX spectra.

2.3. Combining the Optical and Infrared Spectra

The near-infrared spectra were extended blueward to $\sim 0.6 \mu\text{m}$ using published red-optical spectra. These spectra, which cover from roughly 0.6 to $0.95 \mu\text{m}$ and typically have resolutions ranging from 9 to 18 \AA ($R=890-444$), are from Kirkpatrick et al. (1991, 1999, 2000), Tinney & Reid (1998), Martín et al. (1999), Fan et al. (2000), Gizis et al. (2000), Reid et al. (2000), Burgasser et al. (2003) and T. Henry (2004, private communication). For each dwarf, the wavelengths of the optical spectrum were converted from air to vacuum if necessary. The optical spectrum was scaled to the same flux level as the flux-calibrated SpeX spectrum and linearly interpolated onto the wavelength grid of the SpeX spectrum. The two spectra were then combined using a mean. Since many of the optical spectra have not been corrected for telluric absorption, care was taken to scale the spectra using wavelength ranges with a minimal amount of telluric absorption, namely $0.81-0.83 \mu\text{m}$ and $0.99-1.05 \mu\text{m}$.

Figure 1 shows a subset of the flux calibrated $0.6-4.1 \mu\text{m}$ spectra of the dwarfs listed in Table 1. The S/N of the spectra in the J , H , and K bands ranges from ~ 50 in the T dwarfs to ~ 200 in the M dwarfs. The S/N in the L' band is typically lower ranging from ~ 10 in the T dwarfs to ~ 100 in the M dwarfs.

3. Analysis

3.1. Feature Identifications

The identification of atomic and molecular absorption features in the spectra of M, L, and T dwarfs is important because they can be used to constrain the effective temperatures (T_{eff}), surface gravities ($\log g$), and metallicities ($[M/H]$) of the dwarfs. In addition, the process allows the identification of opacity sources not currently included in atmospheric models. There have been numerous infrared spectroscopic studies that identify both atomic and molecular absorption features in the spectra of M, L, and T dwarfs (e.g., Jones et al. 1994; Ali et al. 1995; Leggett et al. 1996; McLean et al. 2000; Reid et al. 2001; Burgasser et al. 2000, 2002a). However, the quality of the identifications ranges from secure to questionable because in some cases, the spectra have low spectral resolution, low S/N, small wavelength coverage and/or sparse spectral type coverage. Since our data do not suffer from these shortcomings, we have conducted a systematic search for both atomic and molecular features in our M, L, and T dwarf spectra. We have confined our search to $\lambda \gtrsim 0.95 \mu\text{m}$ since Kirkpatrick et al. (1991, 1995, 1999) have adequately identified the atomic and molecular features in the spectra of ultracool dwarfs shortward of this wavelength.

We describe the identification of the molecular and atomic features in the following two subsections. Many of the features are weak and could easily be mistaken for noise. However, we are confident in our identifications because the features can be tracked through the spectral sequence. Tables 5 lists the identified molecular features while Table 6 lists the identified atomic features.

Finally, we avoid the use of the term ‘lines’ since at $R \approx 2000$, many of the features, especially the molecular ones, are blends of many individual lines.

3.1.1. Molecular Features

TiO. — Absorption bands of TiO that arise from the γ ($A^3\Phi - X^3\Delta$), γ' ($B^3\Pi - X^3\Delta$), δ ($b^1\Pi - a^1\Delta$) and ϵ ($E^3\Pi - X^3\Delta$) systems are prominent in the red-optical spectra of mid- to late-type M stars (e.g., Kirkpatrick et al. 1991; Tinney & Reid 1998) and early-type L dwarfs (Kirkpatrick et al. 1999). The ϕ ($b^1\Pi - d^1\Sigma$) system has also been detected in the spectra of giant stars (Joyce et al. 1998) but never, to our knowledge, in the spectra of dwarf stars. However, synthetic spectra of M dwarfs computed from the model atmospheres of Allard et al. (2000) predict a strong 0–0 bandhead at $\sim 1.104 \mu\text{m}$.

We have compared the high-resolution ($R=800,000$) Fourier Transform Spectrometer (FTS) emission spectrum³ of TiO used in the analysis of the ϕ system by Galehouse et al. (1980) to our M and L dwarf spectra in order to determine to what extent the 0–0 band of the ϕ system is present. We smoothed the TiO spectrum to $R = 2000$ and then resampled it onto the wavelength grid of the dwarfs. We find no evidence of absorption due to the 0–0 band in the spectra of the M and L dwarfs.

VO. — Absorption bands of VO arising from the $B^4\Pi - X^4\Sigma^-$ system are prominent in the red-optical spectra of late-type M dwarfs (Kirkpatrick et al. 1991, 1995; Tinney & Reid 1998). The $A^4\Pi - X^4\Sigma^-$ system produces three bands, the 1–0 at $\sim 0.96 \mu\text{m}$, the 0–0 at $\sim 1.06 \mu\text{m}$, and the 0–1 at $1.18 \mu\text{m}$. The 0–0 and 0–1 bands and their associated bandheads have been detected in the spectra of M giants (e.g., Joyce et al. 1998); the 1–0 band is difficult to detect because of contamination by telluric H_2O absorption. Kirkpatrick et al. (1993) identified the 0–0 band in the spectrum of vB 8 (M7 V) and Kirkpatrick et al. (1999) claimed to detect this band in the spectrum of GD 165 B (L4). However, the Kirkpatrick et al. spectrum of GD 165 B is missing the wavelengths centered on the 0–0 band of VO which casts doubt on the identification.

We have compared our spectrum of vB 10 (M8 V) with a high-resolution FTS emission spectrum of VO kindly provided S. Davis (2002, private communication) in order to confirm the presence of the 0–0 band of VO in the spectra of M and L dwarfs. The FTS spectrum was smoothed to $R = 2000$ and then resampled onto the wavelength grid of vB 10. Figure 2 shows the spectrum of vB 10 in the top panel and the emission spectrum of VO in the lower panel. It is apparent that the broad feature in the vB 10 spectra centered at $1.06 \mu\text{m}$ is due to the 0–0 band of VO. However, almost all of the high frequency features seen in the vB 10 spectrum have been ascribed to FeH (Cushing et al. 2003). It may be that some of the features in this wavelength range identified as

³We obtained the spectrum (770629R0.005) using the National Solar Observatory Digital Library Query Tool, http://diglib.nso.edu/nso_user.html

FeH are actually a blend of both FeH and VO lines.

In order to quantify the variation of the strength of this band as a function of spectra type, we followed Kirkpatrick et al. (1995) and defined a spectral index that measures the ratio of the flux density in the band to the expected flux density at the same wavelength based on a linear interpolation between continuum points on either side of the band. This index is given by,

$$z\text{-VO} = \frac{0.4667f_{1.084} + 0.5334f_{1.039}}{f_{1.06}}, \quad (3)$$

where f_{λ_0} is the mean flux density in a $0.008 \mu\text{m}$ window centered around λ_0 . Larger values of $z\text{-VO}$ imply deeper absorption. The VO indices computed for the dwarfs in our sample are shown as a function of spectral types in Figure 3. The error bars were computed from the uncertainties in the mean flux densities in $f_{1.039}$, $f_{1.06}$, and $f_{1.084}$. The VO band first appears at a spectral type of $\sim\text{M6}$, peaks in strength at $\sim\text{L0}$, and disappears by $\sim\text{L5}$. The strengths of the 1–0 and 0–0 bands of the $B^4\Pi - X^4\Sigma^-$ system peak at $\sim\text{M9}$ (Kirkpatrick et al. 1999), which lends further credence to the idea that the broad feature at $1.06 \mu\text{m}$ is carried by VO. Given that the Kirkpatrick et al. GD 165B spectrum is missing the wavelengths centered on this band, this is the first detection of the 0–0 band of the $A^4\Pi - X^4\Sigma^-$ transition of VO in the spectra of L dwarfs.

CrH. — The appearance of the CrH bandhead, which arises from the 0–0 band of the $A^6\Sigma^+ - X^6\Sigma^+$ system, at $0.8611 \mu\text{m}$ in the spectra of late-type dwarfs is one of the defining characteristics of the L spectral class (Kirkpatrick et al. 1999; Martín et al. 1999). Although the 0–1 bandhead of the same system at $\sim 0.9969 \mu\text{m}$ is also often identified in the spectra of late-type dwarfs, Cushing et al. (2003) have shown that in $R = 2000$ spectra many of the absorption features near this wavelength can be attributed to the 0–0 band of the $F^4\Delta - X^4\Delta$ system of FeH. As a result, the extent to which the 0–1 band is present in the spectra of late-type dwarfs remains uncertain until higher resolution spectra can be obtained.

Burrows et al. (2002) have computed new line lists and opacities for 12 bands of the $A^6\Sigma^+ - X^6\Sigma^+$ system of CrH. In addition to the 0–0 and 0–1 bands, this system also has bands in the near-infrared at $\sim 1.18 \mu\text{m}$ (0–2) and $\sim 1.4 \mu\text{m}$ (0–3). The 0–3 band will be difficult to identify because it falls within the strong water absorption band, both telluric and intrinsic to the dwarfs, centered at the same wavelength. In order to determine the extent to which the 0–2 band is present in the spectra of L dwarfs, we have compared the CrH cross-section spectrum of Burrows et al. (2002) with the J -band spectrum of 2MASS 1507–1627 (L5). We chose an L5 dwarf to maximize our chances of identifying any CrH features since the strength of the 0–0 band at $0.8611 \mu\text{m}$ peaks at this spectral type (Kirkpatrick et al. 1999). Nevertheless we find no evidence of CrH absorption features in the J -band spectrum of 2MASS 1507–1627. Burgasser et al. (2003) noted that the weakness of the CrH band at $0.9969 \mu\text{m}$ in L dwarf spectra is probably due to the low CrH/FeH equilibrium abundance ratio of $\sim 10^{-3}$ for $1800 \leq T_{\text{eff}} \leq 2500 \text{ K}$ (Lodders 1999) since the cross-sections of FeH and CrH are approximately equal at $0.99 \mu\text{m}$. A similar effect may occur in the J band since the 0–1 band of FeH at $\sim 1.19 \mu\text{m}$ is strong in the spectra of L dwarfs (Cushing et al.

2003; McLean et al. 2003) and the cross-sections of CrH and FeH are also approximately equal at these wavelengths (Dulick et al. 2003).

CH₄. — The appearance of overtone and combination bands of CH₄ in the near-infrared spectra of late-type dwarfs is the defining characteristic of the T spectral class (Burgasser et al. 2002a). For the most part, published spectra of T dwarfs have low spectral resolution so the absorption bands appear relatively smooth. At a resolving power of $R \approx 1200$, it should be possible to identify individual CH₄ absorption features. To this end, we have compared an FTS emission spectrum of CH₄ (Nassar & Bernath 2003) with our spectrum of 2MASS 0559–1404 (T5.0) to search for any common features. The CH₄ spectrum, which was obtained at a temperature of 1000 K, covers from 1.56 to 5.0 μm at a resolving power of $R \approx 160,000$. We smoothed the CH₄ spectrum to $R = 1200$ and resampled it onto the wavelength grid of 2MASS 0559–1404.

Figure 4 shows the spectra of CH₄ and 2MASS 0559–1404 (T5) centered on the $2\nu_3$ band ($\sim 1.6 \mu\text{m}$). Nineteen features common to the two spectra are shown as dotted lines and are listed in Table 7. Although the spectra of the T dwarfs exhibit a series of roughly equidistant absorption features from 1.615 to 1.65 μm , the same series of emission features in the CH₄ spectrum is truncated at $\sim 1.635 \mu\text{m}$. In addition, the strong absorption feature in the T dwarf spectra at 1.665 μm is missing in the CH₄ emission spectrum. The lack of emission of features at these wavelengths is most likely caused by self-absorption due to room temperature CH₄ in the apparatus (Nassar & Bernath 2003). These features can also be seen throughout the T dwarf sequence (McLean et al. 2003).

The Q-branch of the ν_3 fundamental band of CH₄ at 3.33 μm has also been detected in the spectra of two late-type L dwarfs, 2MASS 1507–1627 (L5) and 2MASS 0825+2115 (L7.5), by Noll et al. (2000). Although the detection is secure, the spectra were of fairly low S/N. Figure 5 shows the emission spectrum of CH₄ in the lower panel and the spectra of 2MASS 0825+2115 and SDSS 1254–0122 (T2) in the upper panels, respectively. The dwarf spectra ($R \approx 300$) were obtained using the IRCS on Subaru (see §2.2) and have a higher S/N than the Noll et al. (2000) spectra. The Q-branch is clearly seen in both dwarf spectra while the broad P and R branches can be seen in the spectrum of SDSS 1254–0122.

3.1.2. Atomic Features

In order to identify the atomic features in the spectra of the M and L dwarfs, we used the high-resolution ($R=100,000$) infrared spectral atlas of Arcturus (Hinkle et al. 1995) and a spectrum of Arcturus obtained with SpeX. Arcturus’ spectral type is K1.5 III, cool enough that most of the atomic features present in its spectrum will also be present in the spectra of early-type M dwarfs. We first identified absorption features present in both the SpeX Arcturus spectrum and the spectrum of Gl 229A (M1 V), and then searched the Arcturus atlas for the feature identifications. The absorption features, which include neutral lines of Ti, Al, Si, Ca, Fe, Mg, K, and Na, are listed in Table 6 and shown in Figures 6 - 13.

McLean et al. (2000) reported a detection of the Rb I line at $1.3234 \mu\text{m}$ in the spectra of L dwarfs as well as the Cs I line at $1.359 \mu\text{m}$ in the spectrum of 2MASS 1507–1627 (L5). We see no evidence of these lines nor of any other lines of Rb and Cs (Fisher et al. 1959) in our spectra. There is an absorption feature at $1.3234 \mu\text{m}$ coincident with the position of a Rb line but this feature can be seen in the spectrum of vB 10 (M8 V) and therefore is most likely due to H_2O .

3.2. Spectral Morphology

Having identified both atomic and molecular absorption features in the spectra of the M, L, and T dwarfs, we now give a detailed description of the spectral morphology of the spectra in the z -, J -, H -, K -, and L -bands. Figures 6 - 13 show a sequence of the M, L and T dwarfs in each of the z -, J -, H -, K - and L -bands along with the identified features.

3.2.1. z Band

The z -band spectra of the early M dwarfs contain mainly atomic absorption features of Ti, Fe, Ca, Si, and Mg. Most prominent is a series of 12 Ti features centered at $0.97 \mu\text{m}$ arising from the $a^5\text{F} - z^5\text{F}^\circ$ multiplet. These features are clearly discernible down to a spectral type of M9 and disappear at $\sim\text{L1}$. The band head of the Wing-Ford band of FeH (0–0 band of the $F^4\Delta - X^4\Delta$ system) at $0.9969 \mu\text{m}$, along with the FeH Q-branch feature at $1.006 \mu\text{m}$, already appear quite strong at a spectral type of M1. At later spectral types, the Wing-Ford band replaces the atomic features as the dominant carrier of absorption features in this wavelength range. We have identified 32 FeH features in this wavelength range (Cushing et al. 2003). These features, along with the 0–0 bandhead and Q-branch feature, weaken considerably by a spectral type of $\sim\text{L7}$. The bandhead is also present in the spectrum of the T5 dwarf 2MASS 0559–1404 (see Burgasser et al. (2002b)). The 0–0 band of the $A^4\Pi - X^4\Sigma^-$ system of VO at $\sim 1.06 \mu\text{m}$ appears at a spectral type of $\sim\text{M5}$, peaks in strength at M9, and then disappears by L5 (see §3.1.1). Finally the overall spectral shape becomes progressively redder with spectral type.

3.2.2. J Band

The J band contains the most prominent atomic features in the spectra of M and L dwarfs: the Na doublet at $1.14 \mu\text{m}$, and the two K doublets at 1.175 and $1.25 \mu\text{m}$. Early M dwarf spectra also exhibit absorption features due to Fe, Mg, Ti, Si, H, and Mn but most of these features weaken in the mid- to late-type M dwarfs. However, the Fe feature at $1.189189 \mu\text{m}$ persists to a spectral type of $\sim\text{L5}$. The 0–1 bandhead of FeH ($F^4\Delta - X^4\Delta$ system) at $1.1939 \mu\text{m}$ and the associated Q-branch feature at $1.22210 \mu\text{m}$, along with the 1–2 bandhead at $1.2389 \mu\text{m}$, first appear at a spectral type of M3 and strengthen through the M sequence. Beginning at a spectral type of $\sim\text{M5}$,

33 additional FeH absorption features can also be seen in the range 1.2–1.3 μm (Cushing et al. 2003). At a spectral type of $\sim\text{L1}$, the only remaining atomic features are the Na, and K lines and possibly a few weak Fe features at $\sim 1.155 \mu\text{m}$. The Na feature at 1.14 μm and the FeH features are not apparent at a spectral type of $\sim\text{L7}$ but the K lines persist through the T sequence (McLean et al. 2003). As with the z band, the overall spectral shape of the J band becomes progressively redder with spectral type. Finally, CH_4 bands from 1.15–1.25 μm and CH_4 and H_2O bands longward of 1.28 μm cause the J -band spectra of the T dwarfs to become peaked at $\sim 1.27 \mu\text{m}$.

3.2.3. H Band

The H band is the most difficult wavelength range in which to identify features in the spectra of early M dwarfs because it contains many relatively weak absorption features. Only a few doublets and triplets of Mg, Si, Al, and K are clearly evident. Meyer et al. (1998) identify eight second overtone ($\Delta\nu = 3$) bandheads of ^{12}CO in $R = 3000$ spectra of K and M dwarfs. However, we cannot unambiguously identify any of these bands. H_2O bands on either side of the H -band also begin to appear at a spectral type of $\sim\text{M4}$ and strengthen through the M, L and T sequence.

A new band of FeH, tentatively identified as the $E^4\Pi - A^4\Pi$ system by Wallace & Hinkle (2001), appears at $\sim\text{M5}$ and becomes the dominant carrier of absorption features from 1.59 to 1.75 μm (Cushing et al. 2003). At the same time, the atomic absorption features of Mg, Si, and Al weaken and disappear, except for the K I line at 1.516 μm which persists to $\sim\text{L5}$. Finally, the appearance of the $2\nu_3$ and $2\nu_2 + \nu_3$ bands of CH_4 at $\sim 1.67 \mu\text{m}$ signals the transitions to the T spectral class although weak CH_4 absorption features are also found in the spectra of the late L dwarfs (McLean et al. 2003) (see also §4.2). Both bands strengthen through the T sequence (McLean et al. 2003).

3.2.4. K Band

The K -band spectra of early M dwarfs also exhibit atomic features of Ca, Mg, Al, Si, Na, Ti, and Fe. The most prominent features are the series of Ca lines at 1.95 μm , the Na doublets at 2.21 and 2.34 μm , and the Ca doublet at 2.26 μm . These features all weaken with increasing spectral type; the 2.26 μm Ca doublet disappears at $\sim\text{M7}$, while the 1.95 μm Ca lines, as well as the Na lines, disappear at $\sim\text{L0}$. Also prominent are the series of first overtone band heads ($\Delta\nu = +2$) of ^{12}CO extending redward from 2.29 μm . Beginning with the 6–4 bandhead at 2.41414 μm and moving to lower transitions, the bandheads disappear through the M and L dwarfs until only the 2–0 is present at a spectral type of T2. H_2O absorption bands also appear on either side of the K -band at a spectral type of $\sim\text{M4}$ and strengthen through the M, L, and T sequence. CH_4 absorption at 2.2 μm first appears in the late-type L dwarfs (see also §4.2) and continues to strengthen through the T sequence suppressing the K -band flux. The K -band flux in T dwarfs

is further suppressed by collision-induced H₂ absorption (Borysow 2002). Although this opacity source exhibits no bandheads or distinct spectral features, its presence can be inferred from model atmospheres (M. Marley 2004, private communication) .

3.2.5. *L Band*

The *L*-band spectra of M and L dwarfs are dominated by molecular absorption features due mainly to H₂O. However, there are also absorption features due to the $\Delta\nu = +1$ bands of OH. Features from both the 1–0 and 2–1 bands are seen (Wallace & Hinkle 2002). Like the *z* and *J* bands, the overall slope of the spectra becomes progressively redder with spectral type until the spectra are nearly flat at a spectral type of L1. At a spectral type of \sim L5, the ν_3 fundamental band of CH₄ appears in the spectra (Noll et al. 2000). At first, only the Q-branch is present in the spectra but the P- and R-branches are apparent at T2, and the band becomes saturated by a spectral type of T5.

3.3. Spectral Indices

As described in the previous section, the overall infrared spectral morphology of the M, L, and T dwarfs, as well as the strengths of many of the absorption features including H₂O, FeH, and CO, exhibit a smooth variation with spectral type. To quantify these variations, numerous spectral indices, ratios of fluxes in particular wavelength intervals chosen to measure the changes in spectral morphology or depths of specific absorption features, have been defined (e.g., Tokunaga & Kobayashi 1999; Burgasser et al. 2002a; Geballe et al. 2002; Testi et al. 2001; Reid et al. 2001; McLean et al. 2003). In particular, McLean et al. (2003) have defined a suite of indices for late-type M through T dwarfs (M6 to T8) using spectra with resolving powers similar to that of our spectra ($R=2000$). The H₂OA, H₂OB, H₂OC, and H₂OD indices measure the strength of the 1.35 μm , 1.4 μm , 1.7 μm and 2.0 μm H₂O water bands, respectively, while the *z*-FeH, J-FeH, and CO indices measure the strengths of the 0–0 band of FeH at 0.99 μm , the 0–1 FeH bandhead at 1.17 μm , and the ¹²CO 2–0 bandhead at 2.29 μm , respectively. We have computed these indices for the dwarfs in our sample in order to determine how well they characterize the spectra of dwarfs with spectral types earlier than M6 V. Figure 16 shows the values of the indices as a function of spectral type for the M and L dwarfs in our sample; a smaller value implies stronger absorption.

The H₂OA and H₂OC indices show a good correlation with spectral type throughout the entire M and L sequence. However the continuum flux window for the H₂OA index (1.313 μm) is centered on the Al I doublet at 1.3130514 μm (see §3.4) and as a result, cannot be used for M dwarfs with spectral types earlier than \sim M8. The H₂OB and H₂OD indices are roughly constant from M0 to M4 at which point they decrease steadily through the M, L, T sequence as show by McLean et al. (2003). Also shown in Figure 16 are the best fitting straight lines (solid/dashed) and $\pm 3 \sigma$ errors

(dotted) derived by McLean et al. (2003). All of our data are within the 3σ errors but our H₂OC indices lie systematically below the line defined by McLean et al. It is unclear what causes the systematic differences for the H₂OC index.

The two FeH indices show similar behavior. The indices are roughly constant from M0 to \sim M4 at which point they decrease steadily until a spectral type of \sim L0. The indices are roughly constant from L0 to L5, although there is significant scatter. The FeH bands disappear by the end of the L sequence (the indices approach unity) but the 0–0 band reappears in the mid-type T dwarfs (Burgasser et al. 2002b; McLean et al. 2003). Finally the CO index values, like the H₂OB, H₂D, J -FeH, and z -FeH indices, are roughly constant from M0 to \sim M4 and then decrease through the entire L sequence. The CO index, like the FeH indices, shows significant scatter in the L sequence. Overall, the McLean et al. indices can be used to constrain spectral types only for those dwarfs later than M4.

3.4. Equivalent Widths of Atomic Features

We computed the equivalent widths (EWs) of the strongest atomic features in the spectra of the dwarfs. The EW and the variance of the EW, σ_{EW}^2 , are given by,

$$EW = \sum_{i=1}^n \left[1 - \frac{f(\lambda_i)}{f_c(\lambda_i)} \right] \Delta\lambda_i \quad (4)$$

$$\sigma_{EW}^2 = \sum_{i=1}^n \Delta\lambda_i^2 \left[\frac{\sigma^2(\lambda_i)}{f_c^2(\lambda_i)} + \frac{f^2(\lambda_i)}{f_c^4(\lambda_i)} \sigma_c^2(\lambda_i) \right] \quad (5)$$

where $f(\lambda_i)$ and $f_c(\lambda_i)$ are the observed and estimated continuum flux densities, $\sigma(\lambda_i)$ and $\sigma_c(\lambda_i)$ are the errors in the observed and estimated continuum flux densities, n is the number of wavelength intervals across the feature, and $\Delta\lambda_i$ is the width of wavelength interval i . We estimated $f_c(\lambda_i)$, $\sigma(\lambda_i)$, and $\sigma_c(\lambda_i)$ following the procedure of Sembach & Savage (1992). A linear unweighted polynomial is fitted to the values of the continuum in the regions on either side of the feature in question to determine $f_c(\lambda_i)$. Assuming the fit to be good, $\sigma(\lambda_i)$ is determined *a posteriori* by setting it equal to the standard deviation, s , of the flux density values around $f_c(\lambda_i)$ in the fitting regions. The errors in the continuum, $\sigma_c(\lambda_i)$, are then computed by multiplying the covariance matrix produced by the least-squares fit by s and then using the standard error propagation formula, including the coefficient covariances (see Eqn. A13 of Sembach & Savage 1992).

The strongest atomic features in the spectra of late-type dwarfs are the two K I doublets located at $\sim 1.175\ \mu\text{m}$ and $\sim 1.245\ \mu\text{m}$. Their EWs are tabulated in Table 8 and are shown as a function of spectral type in Figure 17. Although there is some scatter, the EWs of all four lines show a similar behavior with spectral type: they are roughly constant until a spectral type of \sim M4 at which point they increase markedly and reach a maximum at a spectral type of \sim L3. The

EWs then decrease through the late L dwarfs but appear to increase again in the T dwarfs. The strengthening of the K I lines in the early T dwarfs was originally noted by Burgasser et al. (2002a) who ascribed the behavior to the competing effects of decreasing effective temperature and loss of cloud opacity.

We have also computed the EWs of a number of weaker atomic features including the Na doublet at $2.207 \mu\text{m}$, and a number of features from refractory elements, including Al, Mg, Fe, and Ca. Except for the Mg line at $1.183 \mu\text{m}$, all of the features are a blend of a number of lines. Their EWs are tabulated in Table 9 and are shown as a function of spectral type in Figure 18. There is significant scatter but all the lines weaken with increasing spectral type except for the Fe I line at $1.189 \mu\text{m}$ which shows almost no correlation with spectral type. Additionally, all of the lines disappear by a spectral type of $\sim\text{L1}$ except for the Fe I line which persists to $\sim\text{L5}$. The refractory element lines probably weaken in the late-type M dwarfs due to the formation of condensates in the atmospheres of the dwarfs (Lodders 2002) but the effects of decreasing effective temperature may also play a role. Two stars, Gl 411 (M2 V) and Gl 213 (M4 V), have low Fe, Al, Na, and Ca EWs relative to the trend established by the other M dwarfs suggesting they may have low metallicities. The classification of Gl 213 as an old disk-halo star by Leggett (1992) suggests it may have a low metallicity while the metallicity of Gl 411 has been measured to be $[\text{Fe}/\text{H}] = -0.2$ (Mould 1978). We will explore the variations in the EWs of these features more fully in a subsequent paper.

4. Individual Objects of Interest

4.1. 2MASS 2224–0158

2MASS 2224+0158 is classified as L4.5 based on its red-optical spectrum (Kirkpatrick et al. 2000). The $0.6\text{--}4.1 \mu\text{m}$ spectrum of 2MASS 2224–0158 is shown in Figure 19 along with the spectrum of 2MASS 1507–1627, a normal L5 dwarf. The two objects have the same spectral type within the errors (± 0.5 subclass). The 2MASS 1507–1627 spectrum was scaled by the square of the ratio of the distances of the two objects to adjust its flux to the level that would be observed if it were at the distance of 2MASS 2224–0158. The spectrum of 2MASS 2224–0158 is depressed in the *J* and *H* bands relative to that of 2MASS 1507–1627, which results in a very red color $J - K = 2.051$. The ^{12}CO 2–0 and 3–1 bandheads at $\sim 2.3 \mu\text{m}$ in 2MASS 2224–0158 are also considerably deeper than in the spectrum of 2MASS 1507–1627.

Interstellar extinction is probably not the cause of the extremely red color since 2MASS 2224–0158 lies at a distance of ~ 11 pc. An examination of the blue POSS I plates also reveals no obvious extinction in the field of 2MASS 2224–0158. Therefore the extremely red color of 2MASS 2224–0158 appears to be intrinsic to the object and may result from an unusually thick cloud deck, since dwarfs become progressively redder with an increasing column abundance of dust. The CO $\Delta\nu = +2$ bandheads in the spectra of M giant stars are deeper than in the spectra of M dwarfs of the same spectral type (Kleinmann & Hall 1986). If this trend were to continue to cooler

temperatures, the deep CO bands may indicate that 2MASS 2224–0158 has a low surface gravity.

4.2. DENIS 0255–4700 and the L/T Transition

There has been much interest in objects with spectral types at the transition between the L and T dwarfs (McLean et al. 2001; Nakajima et al. 2001; Schweitzer et al. 2002; Geballe et al. 2002; Burgasser et al. 2002a; Tsuji & Nakajima 2003). This interest stems not only from a desire to determine the exact spectral morphological changes that signal the transition to the T spectral class but also to understand why dwarfs at the L/T boundary (L7 to T3) have roughly the same effective temperature (Golimowski et al. 2004).

DENIS 0255–4700 was classified as bdL6 by Martín et al. (1999) and reclassified as \sim L8 by Kirkpatrick et al. (2000). Figure 20 shows the H -band spectra of DENIS 0255–4700 and SDSS 1254–0122 (T2) in the upper panel and the K -band spectra of the same dwarfs in the lower panel. In the H band, the $2\nu_3$ band of CH_4 at $1.67 \mu\text{m}$ is clearly present in the spectrum of DENIS 0255–4700. In addition, the broad absorption trough of the $2\nu_2 + \nu_3$ band centered at $1.63 \mu\text{m}$, along with a number of individual CH_4 features (dotted lines), are also present in the spectrum of DENIS 0255–4700. The K -band spectrum of DENIS 0255–4700 also shows evidence of CH_4 absorption. There is an abrupt slope change in the K -band spectrum at $\sim 2.2 \mu\text{m}$ that is coincident with the absorption maximum of the $\nu_2 + \nu_3$ band. This feature has been seen in other late-type L dwarfs but there has been some disagreement about its carrier. For example, Tokunaga & Kobayashi (1999) ascribe a similar feature in the spectrum of DENIS 0205–11AB to collision-induced H_2 absorption. However, Nakajima et al. (2001) find evidence of CH_4 absorption in both H - and K - band spectra of 2MASS 0902+3517 (L6.5). Given the clear detection of CH_4 features in the H -band, we also ascribe this feature in the spectrum of DENIS 0255–4700 to CH_4 .

Given the detection of CH_4 absorption in the H - and K -band spectra of DENIS 0255–4700, should it be reclassified as a T dwarf? There are two spectral classification schemes currently in use for T dwarfs (Burgasser et al. 2002a; Geballe et al. 2002). The defining characteristic of a T dwarf given by Geballe et al. (2002) is “... the appearance of methane absorption in the H band, i.e., to its earliest appearance in *both* the H and K bands.” By this definition, DENIS 0255–4700 is a T dwarf. However, we have computed the spectral indices for DENIS 0255–4700 defined by Geballe et al. (2002) after smoothing the spectrum to $R \approx 500$ (the resolving power of the spectral standards). All of the Geballe et al. indices indicate DENIS 0255–4700 has a spectral type earlier than T0. The discrepancy probably results from the difference in resolving power; the H -band methane features are simply too difficult to identify in $R \approx 500$ spectrum. Therefore, in the Geballe et al. (2002) classification system, DENIS 0255–4700 should remain a late-type L dwarf.

Finally, Burgasser et al. (2002b) have suggested that late-type L and early-type T dwarfs may exhibit substantial photometric or spectroscopic variability due to the breakup of the cloud decks as they pass into the atmospheric convective zone. As DENIS 0255–4700 is the brightest ($K =$

11.55) late-type L dwarf, it would be an interesting target for both photometric and spectroscopic variability studies.

5. Bolometric Fluxes and Luminosities

The effective temperatures of ultracool dwarfs are typically determined by combining observationally measured bolometric luminosities with theoretical stellar radii (e.g., Leggett et al. 1996, 2001, 2002; Dahn et al. 2002; Golimowski et al. 2004). The bolometric luminosities are measured using absolutely flux-calibrated 1–2.5 μm spectra, L' -band photometry to account for the flux emitted between 2.5 and 3.6 μm , and a Rayleigh-Jeans tail at $\lambda > 3.6 \mu\text{m}$. Although atmospheric models indicate using L' -band photometry is a valid approximation, it has never been tested observationally. Our spectra are ideal for testing this assumption.

In order to construct spectra suitable for integration over all wavelengths, we follow the standard practice of extending the spectra shortward of 0.6 μm using published optical photometry and longward of 4.1 μm using a Rayleigh-Jeans tail (Berriman & Reid 1987; Leggett et al. 1996, 2001). The U , B , and V magnitudes of the M dwarfs (Leggett 1992) were converted to flux densities using the effective wavelength approach described by Leggett et al. (1996). For each dwarf spectrum, we linearly interpolated from zero flux at zero wavelength, through the U -, B -, and V -band flux densities if available, to the flux density at the bluest wavelength of the spectrum. The gaps in each spectrum at 1.85 and 2.6 μm were removed by linear interpolation between the flux densities at the gap edges. Finally, we extended a Rayleigh-Jeans tail from the reddest wavelength of each spectrum to infinity.

Since there are limited observations of ultracool dwarfs at $\lambda > 4\mu\text{m}$, we must resort to model atmospheres to determine the validity of assuming a Rayleigh-Jeans tail at these wavelengths. We have compared the integrated flux of a Rayleigh-Jeans tail and the integrated flux of the NEXTGEN, DUSTY, and COND synthetic spectra (Allard et al. 2001) at various effective temperatures at $\lambda > 4.1 \mu\text{m}$. In gross terms, the NEXTGEN, DUSTY, and COND models are appropriate for M, L, and T dwarfs, respectively. The integrated flux of a Rayleigh-Jeans tail at $\lambda > 4.1 \mu\text{m}$ agrees with that of the models to $\sim 1\%$, $\sim 5\%$, and $\sim 20\%$ for M, L, and T dwarfs, respectively. The large discrepancy between the Rayleigh-Jeans tail and the models appropriate for the T dwarfs (COND) is a result of absorption bands of H_2O , CH_4 , and NH_3 in the 6 to 12 μm region (Roellig et al. 2004).

The integrated bolometric fluxes for the dwarfs with 0.6–4.1 μm spectra are listed in column 3 of Table 10. The errors in the bolometric fluxes include the error due to the photometry used to flux calibrate the spectra and an estimate of the systematic error introduced by assuming a Rayleigh-Jeans tail at $\lambda > 4.1 \mu\text{m}$. Leggett et al. (1996, 2001, 2002) have computed bolometric fluxes for eleven of the M and L dwarfs in our sample. They compute these bolometric fluxes using near-infrared spectroscopy and L' -band photometry as described above. Their bolometric

flux measurements agree with our measurements within the errors for all eleven of the dwarfs. This is not unexpected since the spectra are relatively featureless from 3.42 to 4.12 μm , the wavelengths at which the MKO L' -band filter transmission is 50% of the peak (Tokunaga et al. 2002). The good agreement between the two methods means L' -band photometry can be used as a substitute for L -band spectroscopy greatly simplifying the calculation of the bolometric fluxes of M and L dwarfs. The bolometric luminosities and absolute bolometric magnitudes of the dwarfs with measured parallaxes are also given in columns 5 and 6 of Table 10.

In principle, we could now use the derived bolometric luminosities to determine the effective temperatures of the dwarfs in our sample. However since our L_{bol} measurements agree with those of Leggett et al. (2001), our T_{eff} estimates will also agree and therefore we do not repeat this analysis. We instead refer the reader to the recent work of Golimowski et al. (2004) that determined the effective temperatures of a large sample of ultracool dwarfs using the same technique as Leggett et al. (2001).

6. Summary

We have presented a spectroscopic sequence of M, L, and T dwarfs, cover the wavelength range 0.6 to 4.1 μm , obtained with data from SpeX on the NASA IRTF, the IRCS on the Subaru Telescope, and previously published red-optical spectra. Neutral lines of Al, Fe, Mg, Ca, and Ti are identified in the spectra of the M dwarfs but are all but absent in the spectra of the L dwarfs. Nineteen new weak CH_4 absorption features are identified in the H -band spectrum of 2MASS 0559–1404. We also confirm the presence of the 0–0 band of the $A\ ^4\Pi - X\ ^4\Sigma^-$ transition of VO at $\sim 1.06\ \mu\text{m}$ in the spectra of late-type M dwarfs and detect it for the first time in the spectra of the early-type L dwarfs. No absorption features of Cs, Rb, or CrH, hallmarks of L dwarf spectra in the red-optical, are found at $\lambda > 1.0\ \mu\text{m}$. The suite of spectroscopic indices derived by McLean et al. generally saturate for spectral types earlier than $\sim \text{M4 V}$ thus limiting their usefulness to later spectral types. The bolometric luminosities of the dwarfs in our sample agree with previously published results that make use of L' -band photometry rather than spectroscopy. This results validates the use of L' -band photometry as a substitute for spectroscopy. Finally, 2MASS 2224–0158 (L4.5) has a very red near-infrared spectrum and deep CO bands which may be indicative of low surface gravity and unusually thick condensate clouds. The SpeX spectra can be obtained at the SpeX website <http://irtfweb.ifa.hawaii.edu/Facility/spex/> and the 0.6–4.1 μm spectra are available on request from the primary author.

The authors wish to thank Davy Kirkpatrick, Sandy Leggett, Adam Burgasser, Hugh Jones, Eduardo Martín and Tod Henry and the RECONS team for providing the M, L, and T dwarf optical spectra, Sumner Davis and Ray Nassar for their high-resolution emission spectra of VO and CH_4 , and Mark Marley and Richard Freedman for useful discussions. We also thank the anonymous referee for his/her prompt review of the manuscript. This publication makes use of data from

the Two Micron All Sky Survey, which is a joint project of the University of Massachusetts and the Infrared Processing and Analysis Center, and funded by the National Aeronautics and Space Administration and the National Science Foundation. This research has made use of the SIMBAD database, operated at CDS, Strasbourg, France. M.C.C. acknowledges financial support from the NASA Infrared Telescope Facility and NASA through the Spitzer Space Telescope Fellowship Program.

REFERENCES

- Ali, B., Carr, J. S., Depoy, D. L., Frogel, J. A., & Sellgren, K. 1995, *AJ*, 110, 2415
- Allard, F., Hauschildt, P. H., Alexander, D. R., Tamanai, A., & Schweitzer, A. 2001, *ApJ*, 556, 357
- Allard, F., Hauschildt, P. H., & Schwenke, D. 2000, *ApJ*, 540, 1005
- Auman, J. J. 1967, *ApJS*, 14, 171
- Basri, G., Marcy, G. W., & Graham, J. R. 1996, *ApJ*, 458, 600
- Berriman, G. & Reid, N. 1987, *MNRAS*, 227, 315
- Borysow, A. 2002, *A&A*, 390, 779
- Borysow, A., Jorgensen, U. G., & Zheng, C. 1997, *A&A*, 324, 185
- Burgasser, A. J. 2001, Ph.D. Thesis, Caltech
- Burgasser, A. J., Kirkpatrick, J. D., Brown, M. E., Reid, I. N., Burrows, A., Liebert, J., Matthews, K., Gizis, J. E., Dahn, C. C., Monet, D. G., Cutri, R. M., & Skrutskie, M. F. 2002a, *ApJ*, 564, 421
- Burgasser, A. J., Kirkpatrick, J. D., Liebert, J., & Burrows, A. 2003, *ApJ*, 594, 510
- Burgasser, A. J., Marley, M. S., Ackerman, A. S., Saumon, D., Lodders, K., Dahn, C. C., Harris, H. C., & Kirkpatrick, J. D. 2002b, *ApJ*, 571, L151
- Burgasser, A. J., Wilson, J. C., Kirkpatrick, J. D., Skrutskie, M. F., Colonna, M. R., Enos, A. T., Smith, J. D., Henderson, C. P., Gizis, J. E., Brown, M. E., & Houck, J. R. 2000, *AJ*, 120, 1100
- Burrows, A., Ram, R. S., Bernath, P., Sharp, C. M., & Milsom, J. A. 2002, *ApJ*, 577, 986
- Buser, R. & Kurucz, R. L. 1992, *A&A*, 264, 557
- Chueng, A. S., Taylor, A. W., & Merer, A. J. 1982, *J. Mol. Spect.*, 92, 391
- Cohen, M., Wheaton, W. A., & Megeath, S. T. 2003, *AJ*, 126, 1090

- Cushing, M. C., Rayner, J. T., Davis, S. P., & Vacca, W. D. 2003, *ApJ*, 582, 1066
- Cushing, M. C., Vacca, W. D., & Rayner, J. T. 2004, *PASP*, 116, 362
- Dahn, C. C., Harris, H. C., Vrba, F. J., Guetter, H. H., Canzian, B., Henden, A. A., Levine, S. E., Luginbuhl, C. B., Monet, A. K. B., Monet, D. G., Pier, J. R., Stone, R. C., Walker, R. L., Burgasser, A. J., Gizis, J. E., Kirkpatrick, J. D., Liebert, J., & Reid, I. N. 2002, *AJ*, 124, 1170
- Danielson, R. E. 1966, *ApJ*, 143, 949
- Dulick, M., Bauschlicher, C. W., Burrows, A., Sharp, C. M., Ram, R. S., & Bernath, P. 2003, *ApJ*, 594, 651
- Epchtein, N., de Batz, B., Capoani, L., Chevallier, L., Copet, E., Fouque, P., Lacombe, F., Le Bertre, T., Pau, S., Rouan, D., Ruphy, S., Simon, G., Tiphene, D., Burton, W. B., Bertin, E., Deul, E., Habing, H., Borsenberger, J., Dennefeld, M., Guglielmo, F., Loup, C., Mamon, G., Ng, Y., Omont, A., Provost, L., Renault, J.-C., Tanguy, F., Kimeswenger, S., Kienel, C., Garzon, F., Persi, P., Ferrari-Toniolo, M., Robin, A., Paturel, G., Vauglin, I., Forveille, T., Delfosse, X., Hron, J., Schultheis, M., Appenzeller, I., Wagner, S., Balazs, L., Holl, A., Lepine, J., Boscolo, P., Picazzio, E., Duc, P.-A., & Mennessier, M.-O. 1997, *The Messenger*, 87, 27
- Fan, X., Knapp, G. R., Strauss, M. A., Gunn, J. E., Lupton, R. H., Ivezić, Ž., Rockosi, C. M., Yanny, B., Kent, S., Schneider, D. P., Kirkpatrick, J. D., Annis, J., Bastian, S., Berman, E., Brinkmann, J., Csabai, I., Federwitz, G. R., Fukugita, M., Gurbani, V. K., Hennessy, G. S., Hindsley, R. B., Ichikawa, T., Lamb, D. Q., Lindenmeyer, C., Mantsch, P. M., McKay, T. A., Munn, J. A., Nash, T., Okamura, S., Pauls, A. G., Pier, J. R., Rechenmacher, R., Rivetta, C. H., Sergey, G., Stoughton, C., Szalay, A. S., Szokoly, G. P., Tucker, D. L., York, D. G., & The SDSS Collaboration. 2000, *AJ*, 119, 928
- Fisher, R. A., Knopf, W. C., & Eshbach Kinney, F. 1959, *ApJ*, 130, 683
- Galehouse, D. C., Davis, S. P., & Brault, J. W. 1980, *ApJS*, 42, 241
- Geballe, T. R., Knapp, G. R., Leggett, S. K., Fan, X., Golimowski, D. A., Anderson, S., Brinkmann, J., Csabai, I., Gunn, J. E., Hawley, S. L., Hennessy, G., Henry, T. J., Hill, G. J., Hindsley, R. B., Ivezić, Ž., Lupton, R. H., McDaniel, A., Munn, J. A., Narayanan, V. K., Peng, E., Pier, J. R., Rockosi, C. M., Schneider, D. P., Smith, J. A., Strauss, M. A., Tsvetanov, Z. I., Uomoto, A., York, D. G., & Zheng, W. 2002, *ApJ*, 564, 466
- Gizis, J. E., Monet, D. G., Reid, I. N., Kirkpatrick, J. D., Liebert, J., & Williams, R. J. 2000, *AJ*, 120, 1085

- Golimowski, D. A., Leggett, S. K., Marley, M. S., Fan, X., Geballe, T. R., Knapp, G. R., Vrba, F. J., Henden, A. A., Luginbuhl, C. B., Guetter, H. H., Munn, J. A., Canzian, B., Zheng, W., Tsvetanov, Z. I., Chiu, K., Glazebrook, K., Hoversten, E. A., Schneider, D. P., & Brinkmann, J. 2004, *AJ*, 127, 3516
- Goorvitch, D. 1994, *ApJS*, 95, 535
- Hinkle, K., Wallace, L., & Livingston, W. 1995, *PASP*, 107, 1042
- Jones, H. R. A., Longmore, A. J., Allard, F., Hauschildt, P. H., Miller, S., & Tennyson, J. 1995, *MNRAS*, 277, 767
- Jones, H. R. A., Longmore, A. J., Jameson, R. F., & Mountain, C. M. 1994, *MNRAS*, 267, 413
- Jones, H. R. A., Pavlenko, Y., Viti, S., & Tennyson, J. 2002, *MNRAS*, 330, 675
- Joyce, R. R., Hinkle, K. H., Wallace, L., Dulick, M., & Lambert, D. L. 1998, *AJ*, 116, 2520
- Kirkpatrick, J. D., Allard, F., Bida, T., Zuckerman, B., Becklin, E. E., Chabrier, G., & Baraffe, I. 1999, *ApJ*, 519, 834
- Kirkpatrick, J. D., Henry, T. J., & McCarthy, D. W. 1991, *ApJS*, 77, 417
- Kirkpatrick, J. D., Henry, T. J., & Simons, D. A. 1995, *AJ*, 109, 797
- Kirkpatrick, J. D., Kelly, D. M., Rieke, G. H., Liebert, J., Allard, F., & Wehrse, R. 1993, *ApJ*, 402, 643
- Kirkpatrick, J. D., Reid, I. N., Liebert, J., Gizis, J. E., Burgasser, A. J., Monet, D. G., Dahn, C. C., Nelson, B., & Williams, R. J. 2000, *AJ*, 120, 447
- Kleinmann, S. G. & Hall, D. N. B. 1986, *ApJS*, 62, 501
- Kobayashi, N., Tokunaga, A. T., Terada, H., Goto, M., Weber, M., Potter, R., Onaka, P. M., Ching, G. K., Young, T. T., Fletcher, K., Neil, D., Robertson, L., Cook, D., Imanishi, M., & Warren, D. W. 2000, *Proc. SPIE*, 4008, 1056
- Koornneef, J., Bohlin, R., Buser, R., Horne, K., & Turnshek, D. 1986, *Highlights in Astronomy*, 7, 833
- Leggett, S. K. 1992, *ApJS*, 82, 351
- Leggett, S. K., Allard, F., Berriman, G., Dahn, C. C., & Hauschildt, P. H. 1996, *ApJS*, 104, 117
- Leggett, S. K., Allard, F., Geballe, T. R., Hauschildt, P. H., & Schweitzer, A. 2001, *ApJ*, 548, 908
- Leggett, S. K., Allard, F., & Hauschildt, P. H. 1998, *ApJ*, 509, 836

- Leggett, S. K., Geballe, T. R., Fan, X., Schneider, D. P., Gunn, J. E., Lupton, R. H., Knapp, G. R., Strauss, M. A., McDaniel, A., Golimowski, D. A., Henry, T. J., Peng, E., Tsvetanov, Z. I., Uomoto, A., Zheng, W., Hill, G. J., Ramsey, L. W., Anderson, S. F., Annis, J. A., Bahcall, N. A., Brinkmann, J., Chen, B., Csabai, I., Fukugita, M., Hennessy, G. S., Hindsley, R. B., Ivezić, Ž., Lamb, D. Q., Munn, J. A., Pier, J. R., Schlegel, D. J., Smith, J. A., Stoughton, C., Thakar, A. R., & York, D. G. 2000, *ApJ*, 536, L35
- Leggett, S. K., Golimowski, D. A., Fan, X., Geballe, T. R., Knapp, G. R., Brinkmann, J., Csabai, I., Gunn, J. E., Hawley, S. L., Henry, T. J., Hindsley, R., Ivezić, Ž., Lupton, R. H., Pier, J. R., Schneider, D. P., Smith, J. A., Strauss, M. A., Uomoto, A., & York, D. G. 2002, *ApJ*, 564, 452
- Lodders, K. 1999, *ApJ*, 519, 793
- . 2002, *ApJ*, 577, 974
- Martín, E. L., Delfosse, X., Basri, G., Goldman, B., Forveille, T., & Zapatero Osorio, M. R. 1999, *AJ*, 118, 2466
- McLean, I. S., McGovern, M. R., Burgasser, A. J., Kirkpatrick, J. D., Prato, L., & Kim, S. S. 2003, *ApJ*, 596, 561
- McLean, I. S., Prato, L., Kim, S. S., Wilcox, M. K., Kirkpatrick, J. D., & Burgasser, A. 2001, *ApJ*, 561, L115
- McLean, I. S., Wilcox, M. K., Becklin, E. E., Figer, D. F., Gilbert, A. M., Graham, J. R., Larkin, J. E., Levenson, N. A., Teplitz, H. I., & Kirkpatrick, J. D. 2000, *ApJ*, 533, L45
- Mégessier, C. 1995, *A&A*, 296, 771
- Meyer, M. R., Edwards, S., Hinkle, K. H., & Strom, S. E. 1998, *ApJ*, 508, 397
- Monet, D. G., Dahn, C. C., Vrba, F. J., Harris, H. C., Pier, J. R., Luginbuhl, C. B., & Ables, H. D. 1992, *AJ*, 103, 638
- Mould, J. R. 1978, *ApJ*, 226, 923
- Nakajima, T., Oppenheimer, B. R., Kulkarni, S. R., Golimowski, D. A., Matthews, K., & Durrance, S. T. 1995, *Nature*, 378, 463
- Nakajima, T., Tsuji, T., & Yanagisawa, K. 2001, *ApJ*, 561, L119
- Nassar, R. & Bernath, P. 2003, *J. Quant. Spec. Radiat. Transf.*, 82, 279
- Noll, K. S., Geballe, T. R., Leggett, S. K., & Marley, M. S. 2000, *ApJ*, 541, L75
- Noll, K. S., Geballe, T. R., & Marley, M. S. 1997, *ApJ*, 489, L87

- Oppenheimer, B. R., Kulkarni, S. R., Matthews, K., & van Kerkwijk, M. H. 1998, *ApJ*, 502, 932
- Perryman, M. A. C., Lindegren, L., Kovalevsky, J., Hoeg, E., Bastian, U., Bernacca, P. L., Cr ez e, M., Donati, F., Grenon, M., van Leeuwen, F., van der Marel, H., Mignard, F., Murray, C. A., Le Poole, R. S., Schrijver, H., Turon, C., Arenou, F., Froeschl e, M., & Petersen, C. S. 1997, *A&A*, 323, L49
- Phillips, J. G., Davis, S. P., Lindgren, B., & Balfour, W. J. 1987, *ApJS*, 65, 721
- Press, W. H., Teukolsky, S. A., Vetterling, W. T., & Flannery, B. P. 1992, *Numerical Recipes in FORTRAN* (2nd ed.; Cambridge: Cambridge Univ. Press)
- Rayner, J. T., Toomey, D. W., Onaka, P. M., Denault, A. J., Stahlberger, W. E., Vacca, W. D., Cushing, M. C., & Wang, S. 2003, *PASP*, 115, 362
- Rebolo, R., Martin, E. L., Basri, G., Marcy, G. W., & Zapatero-Osorio, M. R. 1996, *ApJ*, 469, L53
- Reid, I. N., Burgasser, A. J., Cruz, K. L., Kirkpatrick, J. D., & Gizis, J. E. 2001, *AJ*, 121, 1710
- Reid, I. N., Kirkpatrick, J. D., Gizis, J. E., Dahn, C. C., Monet, D. G., Williams, R. J., Liebert, J., & Burgasser, A. J. 2000, *AJ*, 119, 369
- Roellig, T. L., Van Cleve, J. E., Sloan, G. C., Wilson, J. C., Saumon, D., Leggett, S. K., Marley, M. S., Cushing, M. C., Kirkpatrick, J. D., Mainzer, A. K., & Houck, J. R. 2004, *ApJS*, 154, 418
- Ruiz, M. T., Leggett, S. K., & Allard, F. 1997, *ApJ*, 491, L107
- Saumon, D., Geballe, T. R., Leggett, S. K., Marley, M. S., Freedman, R. S., Lodders, K., Fegley, B., & Sengupta, S. K. 2000, *ApJ*, 541, 374
- Saumon, D., Marley, M. S., & Lodders, K. 2003a, *astro-ph* 0310805
- Saumon, D., Marley, M. S., Lodders, K., & Freedman, R. S. 2003b, in *IAU Symp. 211, Brown Dwarfs*, ed. E. Mart ın (San Francisco: ASP), 345
- Schweitzer, A., Gizis, J. E., Hauschildt, P. H., Allard, F., Howard, E. M., & Kirkpatrick, J. D. 2002, *ApJ*, 566, 435
- Sembach, K. R. & Savage, B. D. 1992, *ApJS*, 83, 147
- Skrutskie, M. F., Schneider, S. E., Stiening, R., Strom, S. E., Weinberg, M. D., Beichman, C., Chester, T., Cutri, R., Lonsdale, C., Elias, J., Elston, R., Capps, R., Carpenter, J., Huchra, J., Liebert, J., Monet, D., Price, S., & Seitzer, P. 1997, in *The Impact of Large Scale Near-IR Sky Surveys*, ed. F. Garz on, N. Epchtein, A. Omont, W. B. Burton, & P. Persi (Dordrecht: Kluwer), 25

- Testi, L., D’Antona, F., Ghinassi, F., Licandro, J., Magazzù, A., Maiolino, R., Mannucci, F., Marconi, A., Nagar, N., Natta, A., & Oliva, E. 2001, *ApJ*, 552, L147
- Tinney, C. G. & Reid, I. N. 1998, *MNRAS*, 301, 1031
- Tinney, C. G., Reid, I. N., Gizis, J., & Mould, J. R. 1995, *AJ*, 110, 3014
- Tokunaga, A. T. 2000, in *Allen’s Astrophysical Quantities*, ed. A. N. Cox (4th ed.; New York: Springer), 151
- Tokunaga, A. T. & Kobayashi, N. 1999, *AJ*, 117, 1010
- Tokunaga, A. T., Simons, D. A., & Vacca, W. D. 2002, *PASP*, 114, 180
- Tsuji, T. & Nakajima, T. 2003, *ApJ*, 585, L151
- Vacca, W. D., Cushing, M. C., & Rayner, J. T. 2003, *PASP*, 115, 389
- van Altena, W. F., Lee, J. T., & Hoffleit, E. D. 1995, *The Yale Parallax Catalog* (4th ed.; New Haven: Yale Univ. Observatory)
- Vrba, F. J., Henden, A. A., Luginbuhl, C. B., Guetter, H. H., Munn, J. A., Canzian, B., Burgasser, A. J., Kirkpatrick, J. D., Fan, X., Geballe, T. R., Golimowski, D. A., Knapp, G. R., Leggett, S. K., Schneider, D. P., & Brinkmann, J. 2004, *AJ*, 127, 2948
- Wallace, L. & Hinkle, K. 2001, *ApJ*, 559, 424
- . 2002, *AJ*, 124, 3393
- Wilson, J. C., Miller, N. A., Gizis, J. E., Skrutskie, M. F., Houck, J. R., Kirkpatrick, J. D., Burgasser, A. J., & Monet, D. G. 2003, in *IAU Symposium*, 197
- York, D. G., Adelman, J., Anderson, J. E., Anderson, S. F., Annis, J., Bahcall, N. A., Bakken, J. A., Barkhouser, R., Bastian, S., Berman, E., Boroski, W. N., Bracker, S., Briegel, C., Briggs, J. W., Brinkmann, J., Brunner, R., Burles, S., Carey, L., Carr, M. A., Castander, F. J., Chen, B., Colestock, P. L., Connolly, A. J., Crocker, J. H., Csabai, I., Czarapata, P. C., Davis, J. E., Doi, M., Dombeck, T., Eisenstein, D., Ellman, N., Elms, B. R., Evans, M. L., Fan, X., Federwitz, G. R., Fiscelli, L., Friedman, S., Frieman, J. A., Fukugita, M., Gillespie, B., Gunn, J. E., Gurbani, V. K., de Haas, E., Haldeman, M., Harris, F. H., Hayes, J., Heckman, T. M., Hennessy, G. S., Hindsley, R. B., Holm, S., Holmgren, D. J., Huang, C., Hull, C., Husby, D., Ichikawa, S., Ichikawa, T., Ivezić, Ž., Kent, S., Kim, R. S. J., Kinney, E., Klaene, M., Kleinman, A. N., Kleinman, S., Knapp, G. R., Korienek, J., Kron, R. G., Kunszt, P. Z., Lamb, D. Q., Lee, B., Leger, R. F., Limmongkol, S., Lindenmeyer, C., Long, D. C., Loomis, C., Loveday, J., Lucinio, R., Lupton, R. H., MacKinnon, B., Mannery, E. J., Mantsch, P. M., Margon, B., McGehee, P., McKay, T. A., Meiksin, A., Merelli, A., Monet, D. G., Munn, J. A., Narayanan, V. K., Nash, T., Neilsen, E., Neswold, R., Newberg, H. J.,

Nichol, R. C., Nicinski, T., Nonino, M., Okada, N., Okamura, S., Ostriker, J. P., Owen, R., Pauls, A. G., Peoples, J., Peterson, R. L., Petravick, D., Pier, J. R., Pope, A., Pordes, R., Prosapio, A., Rechenmacher, R., Quinn, T. R., Richards, G. T., Richmond, M. W., Rivetta, C. H., Rockosi, C. M., Ruthmansdorfer, K., Sandford, D., Schlegel, D. J., Schneider, D. P., Sekiguchi, M., Sergey, G., Shimasaku, K., Siegmund, W. A., Smee, S., Smith, J. A., Snedden, S., Stone, R., Stoughton, C., Strauss, M. A., Stubbs, C., SubbaRao, M., Szalay, A. S., Szapudi, I., Szokoly, G. P., Thakar, A. R., Tremonti, C., Tucker, D. L., Uomoto, A., Vanden Berk, D., Vogeley, M. S., Waddell, P., Wang, S., Watanabe, M., Weinberg, D. H., Yanny, B., & Yasuda, N. 2000, *AJ*, 120, 1579

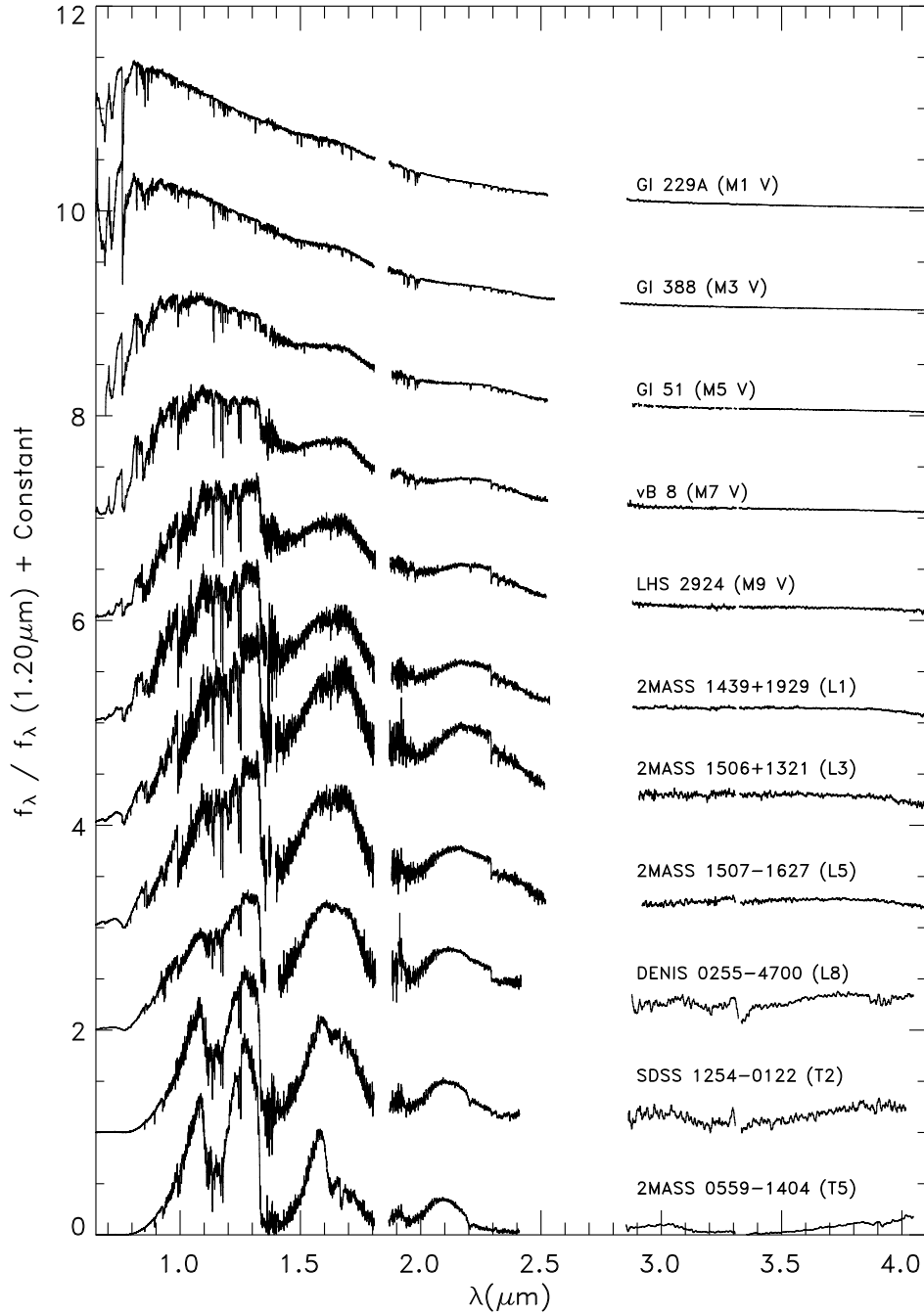


Fig. 1.— 0.6 to 4.2 μm sequence of M, L and T dwarfs. The gaps in the spectra at $\sim 1.85 \mu\text{m}$ are due to a break in the wavelength coverage of the SXD mode of SpeX. The spectra from 2.5 to 2.9 μm were removed because the atmosphere is opaque at these wavelengths.

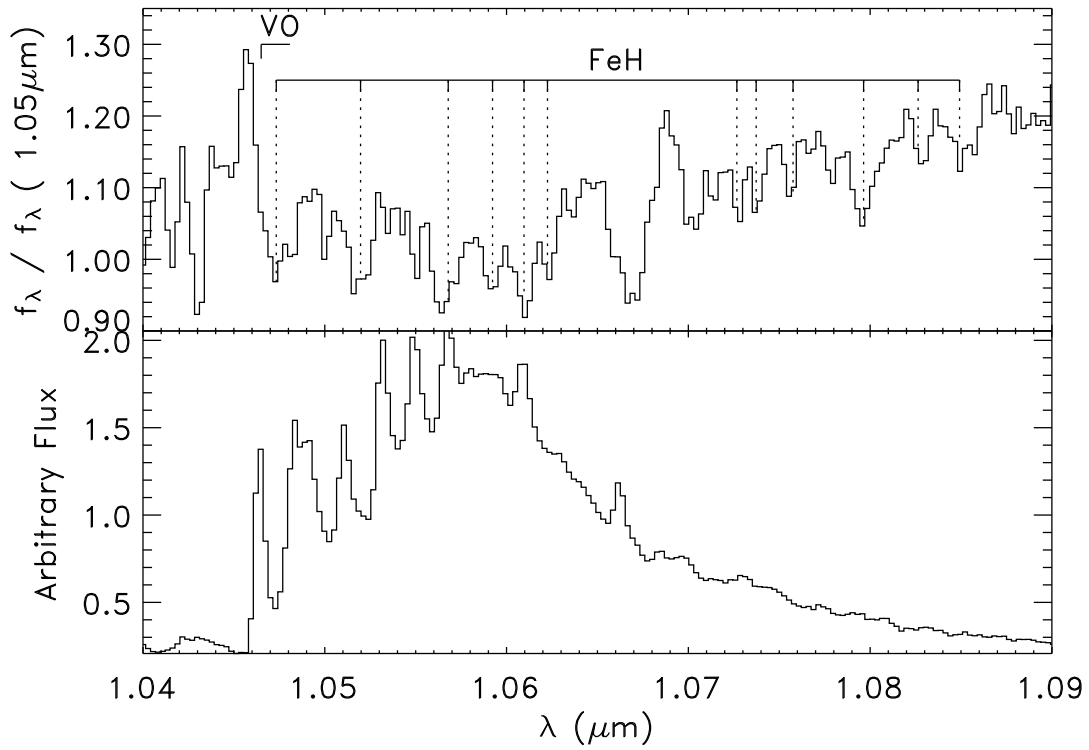


Fig. 2.— The lower panel shows the VO emission spectrum and the upper panel is the spectrum of vB 10 (M8 V). FeH features previously identified are indicated with dotted lines. The broad absorption feature in the spectrum of vB 10 is due to VO.

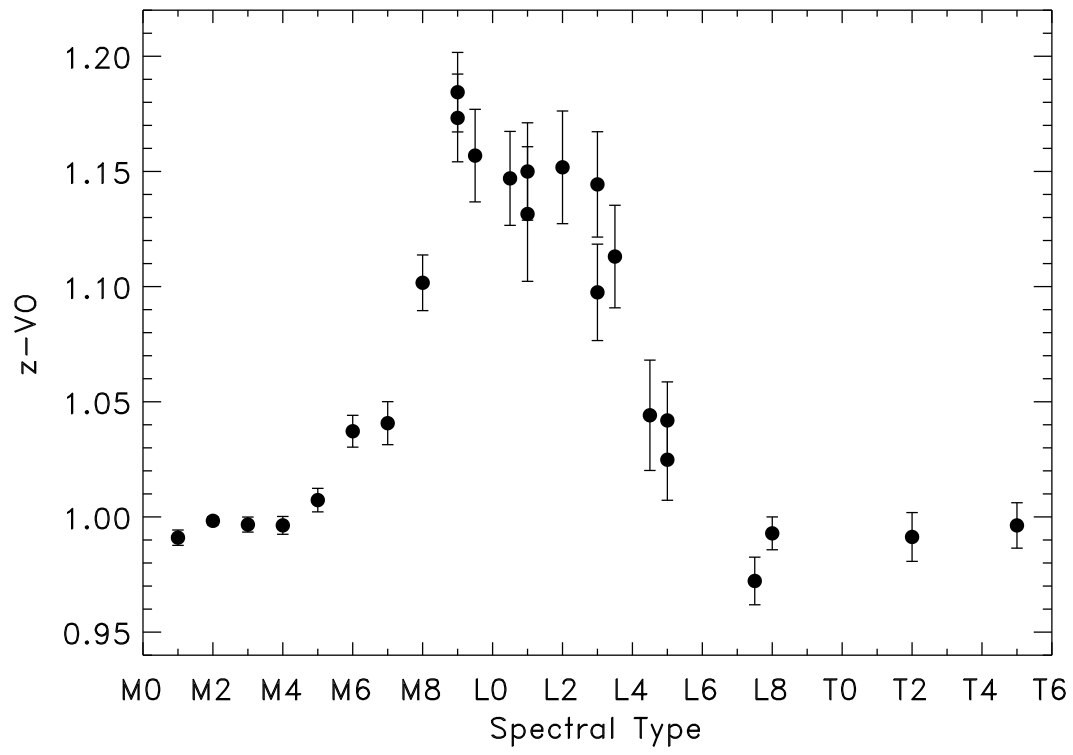


Fig. 3.— The $z-VO$ index as a function of spectral type.

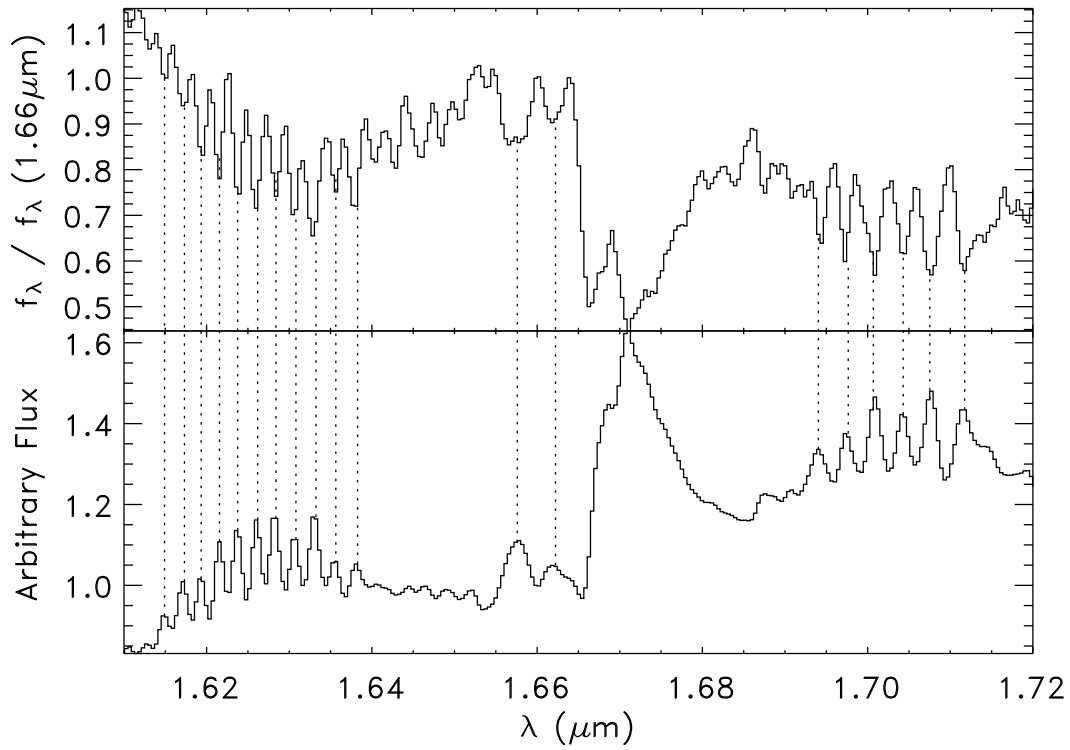


Fig. 4.— The lower panel shows the CH_4 emission spectrum and the upper panel shows the spectrum of 2MASS 0559–1404 (T5) centered on the $2\nu_3$ band. The positions of the 19 features common to both spectra are indicated with dotted lines.

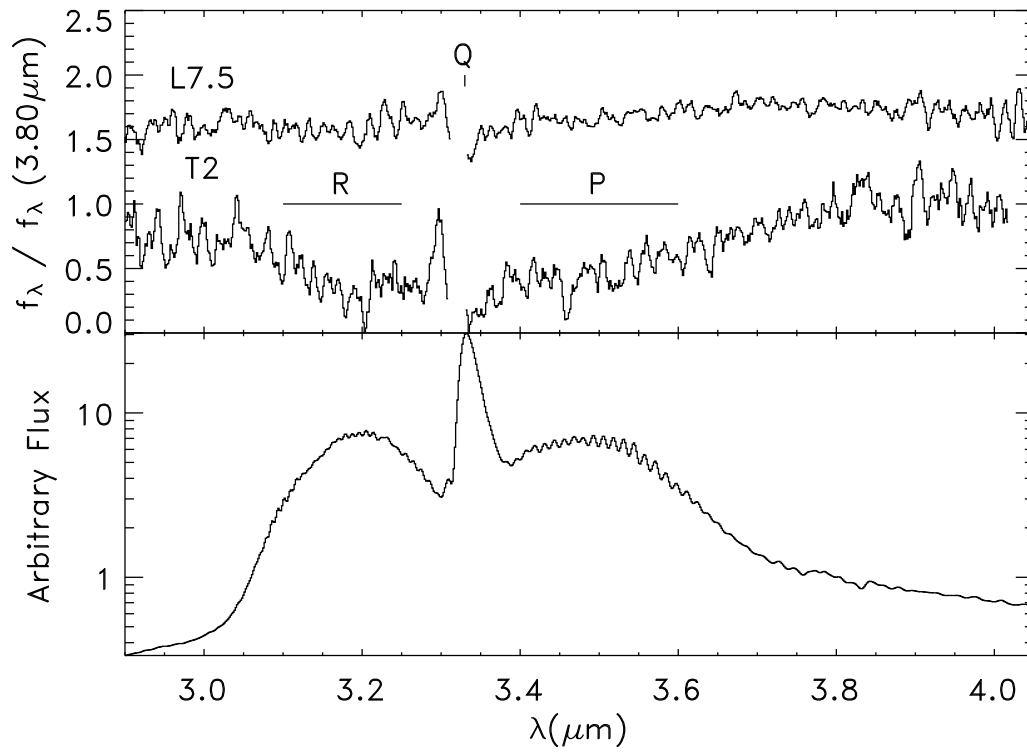


Fig. 5.— The lower panel shows the CH_4 emission spectrum and the upper panel shows the spectra of 2MASS 0825+2115 (L7.5) and SDSS 1254–0122 (T2). Note the CH_4 spectrum is plotted on a logarithmic scale. The positions of the P, Q, and R branches are indicated.

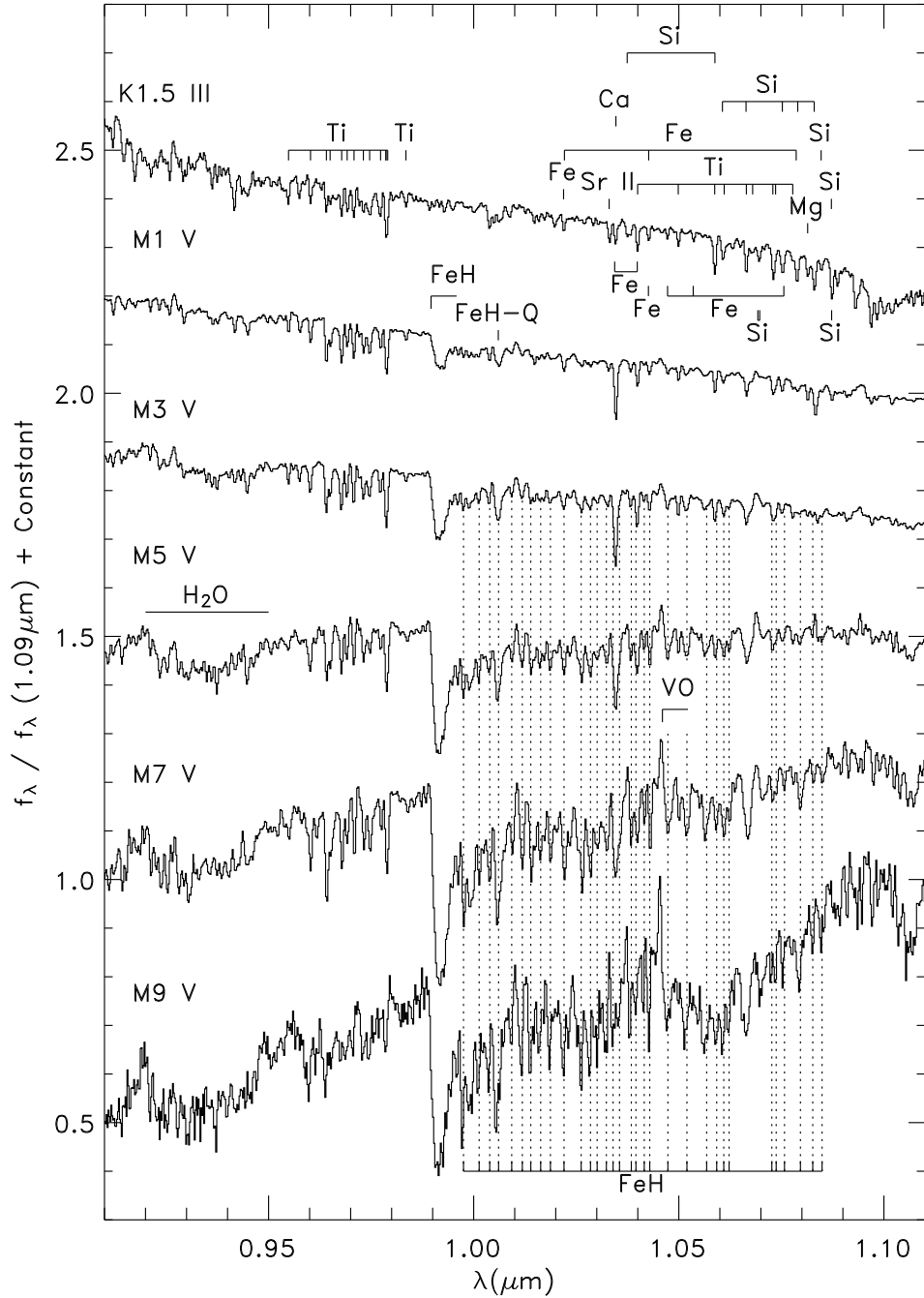


Fig. 6.— z-band spectra of Arcturus (K1.5 III), Gl 229A (M1 V), Gl 388 (M3 V), Gl 51 (M5 V) vB 8 (M7 V) and LHS 2924 (M9 V). The most prominent molecular and atomic features are indicated.

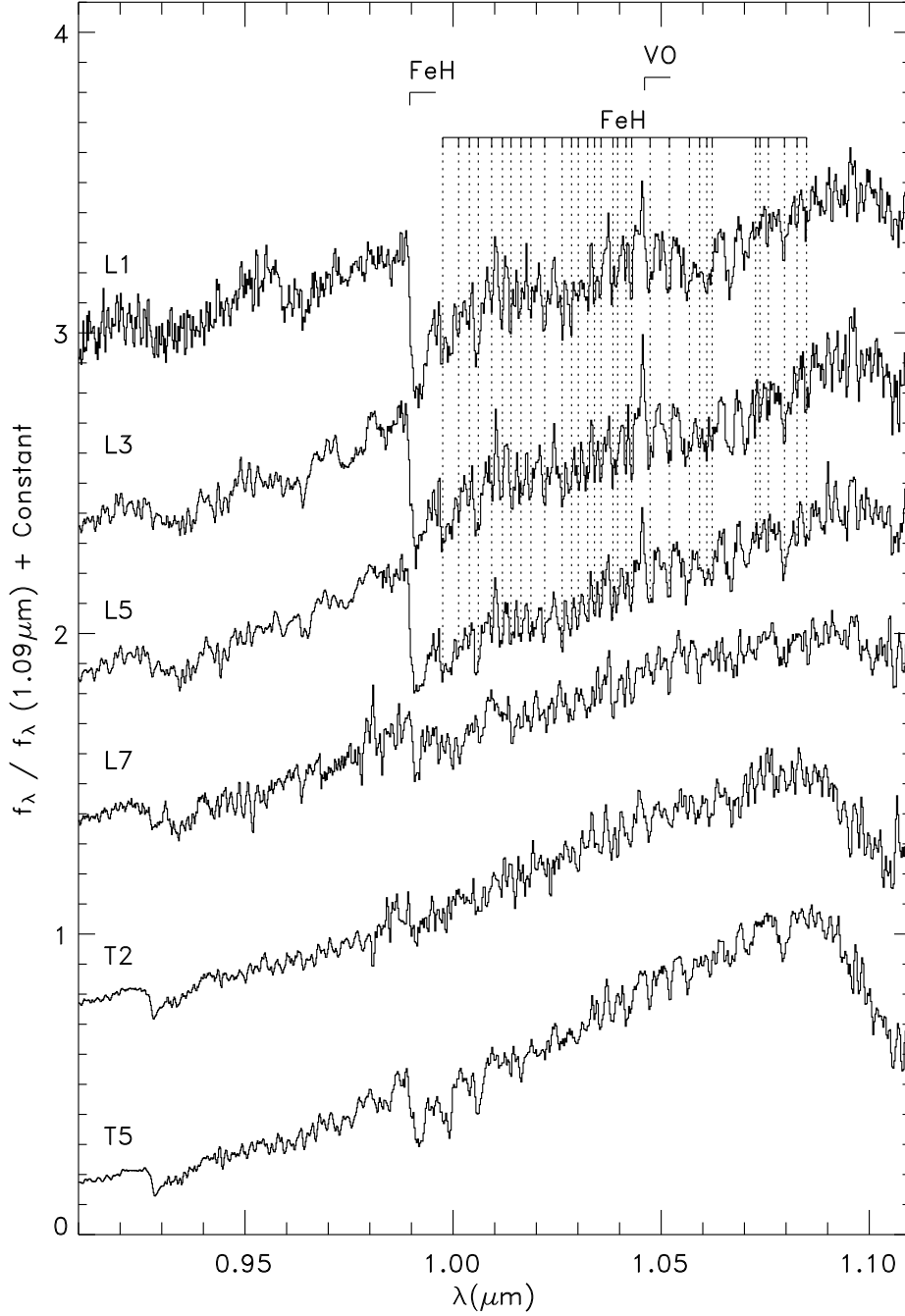


Fig. 7.— z -band spectra of 2MASS1439+1929 (L1), 2MASS 1506+1321 (L3), 2MASS 1507–1627 (L5), DENIS 0255–4700 (L8), SDSS 1254–0122 (T2), and 2MASS 0559–1404 (T5). The most prominent molecular and atomic features are indicated.

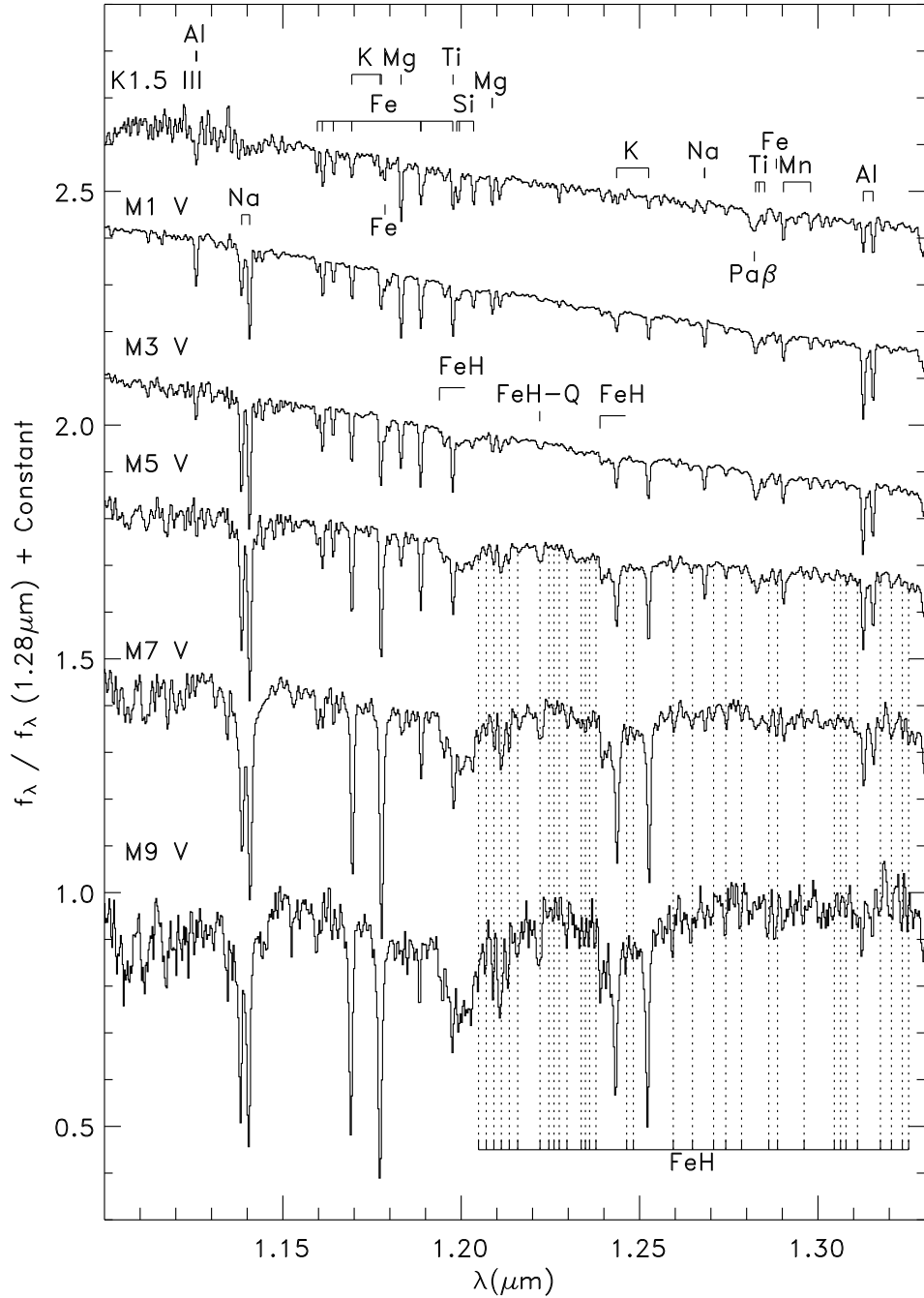


Fig. 8.— *J*-band spectra of Arcturus (K1.5 III), G1 229A (M1 V), G1 388 (M3 V), G1 51 (M5 V) vB 8 (M7 V) and LHS 2924 (M9 V). The most prominent molecular and atomic features are indicated.

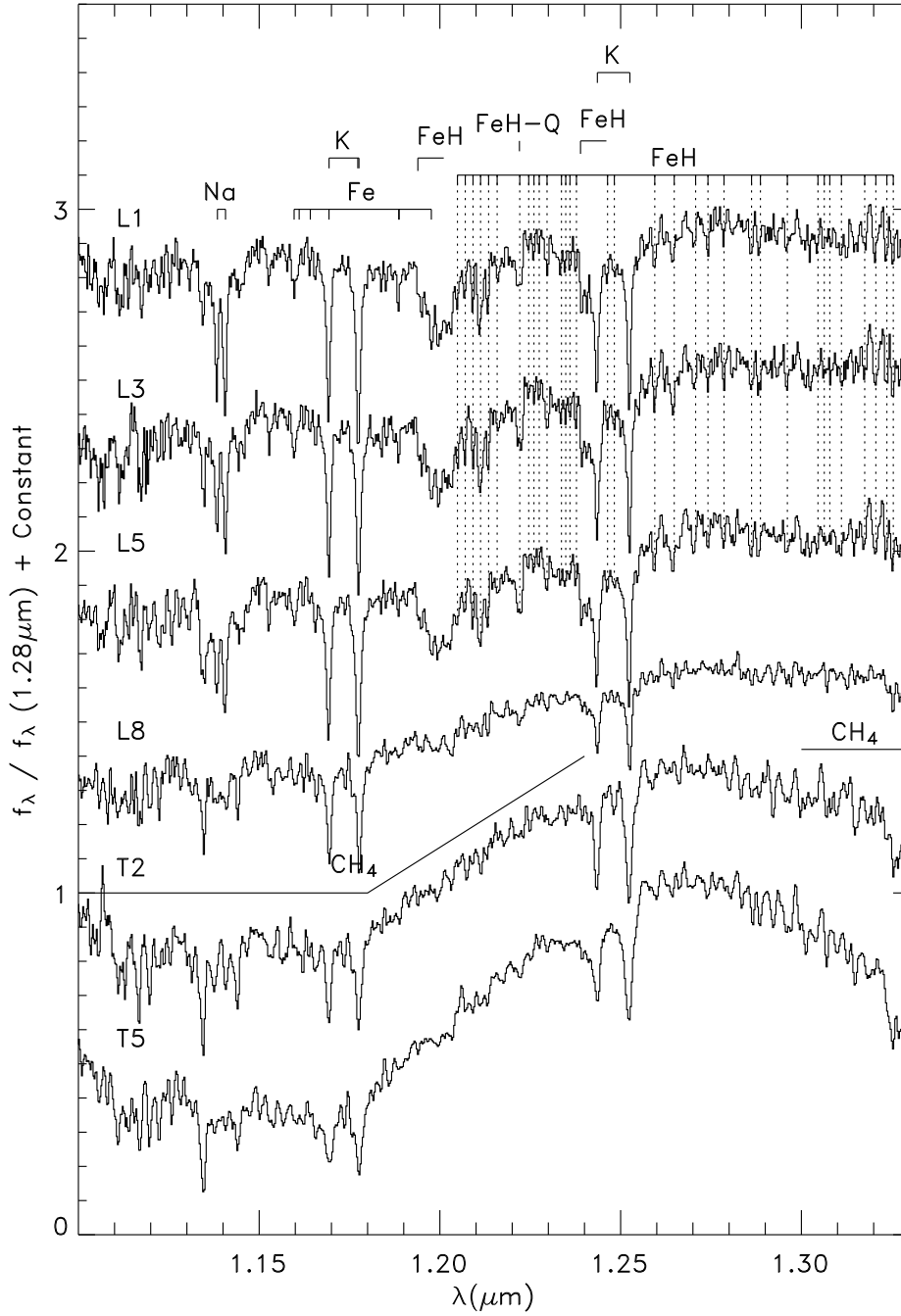


Fig. 9.— *J*-band spectra of 2MASS1439+1929 (L1), 2MASS 1506+1321 (L3), 2MASS 1507–1627 (L5), DENIS 0255–4700 (L8), SDSS 1254–0122 (T2), and 2MASS 0559–1404 (T5). The most prominent molecular and atomic features are indicated.

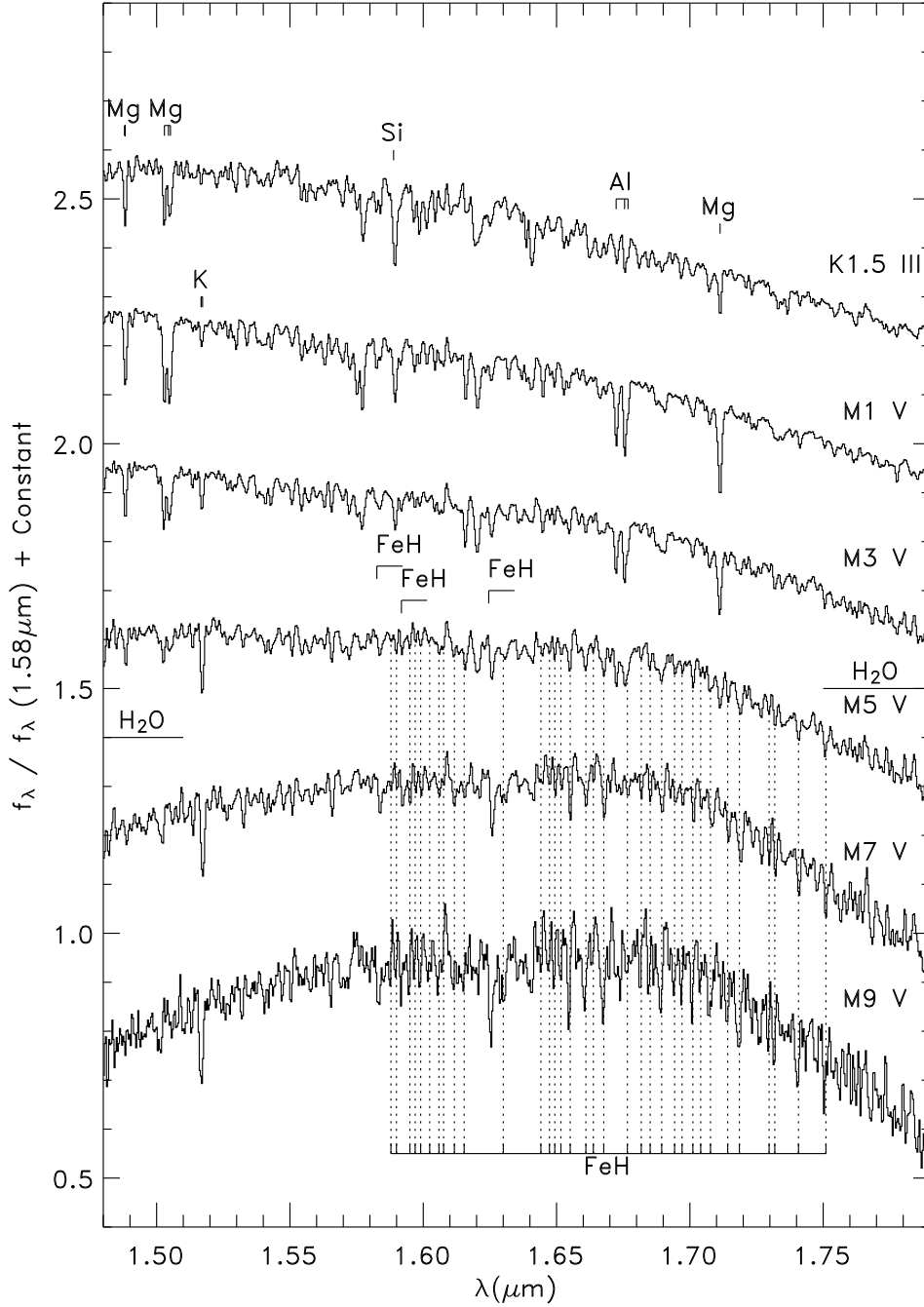


Fig. 10.— *H*-band spectra of Arcturus (K1.5 III), Gl 229A (M1 V), Gl 388 (M3 V), Gl 51 (M5 V) vB 8 (M7 V) and LHS 2924 (M9 V). The most prominent molecular and atomic features are indicated.

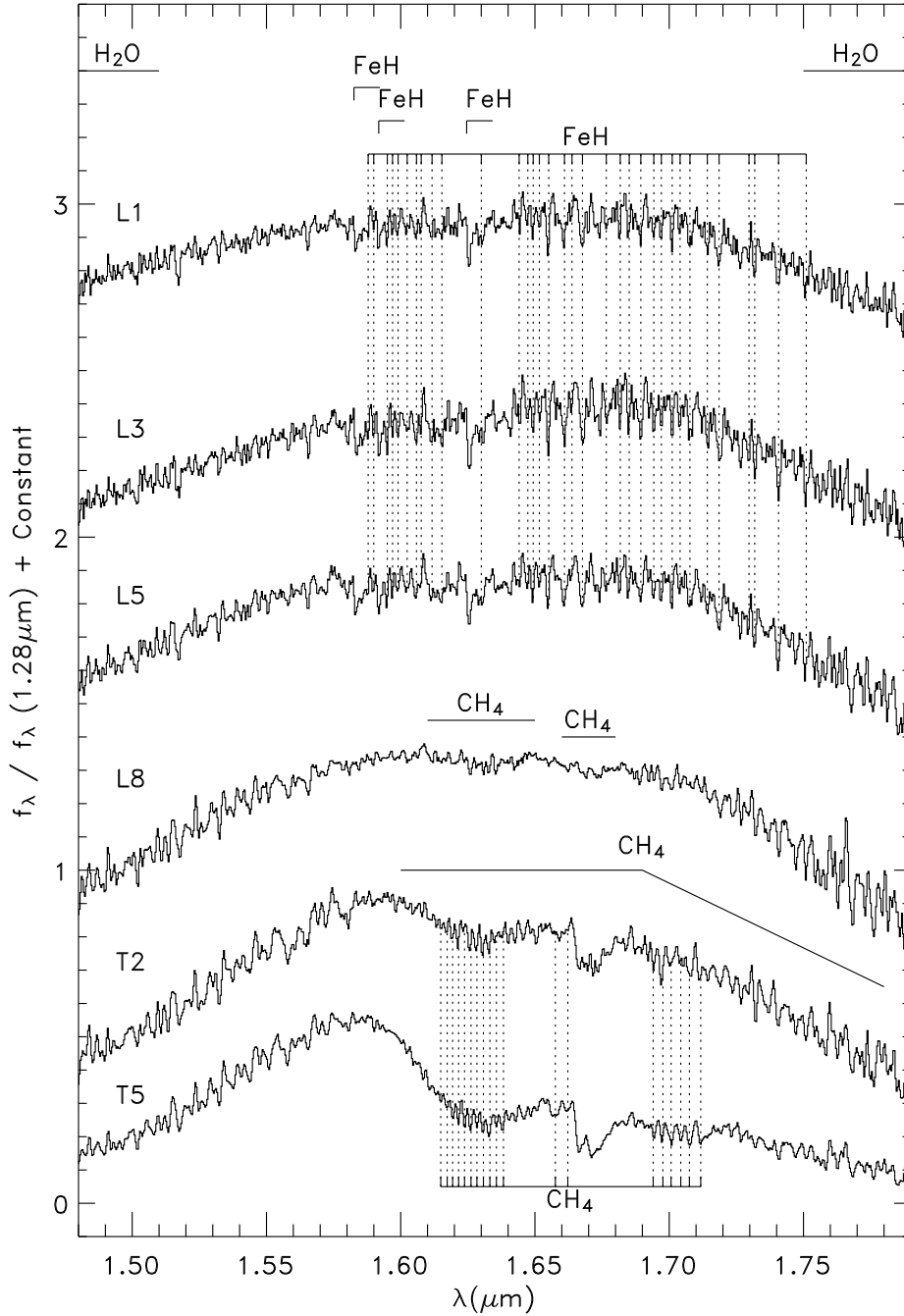


Fig. 11.— *H*-band spectra of 2MASS1439+1929 (L1), 2MASS 1506+1321 (L3), 2MASS 1507–1627 (L5), DENIS 0255–4700 (L8), SDSS 1254–0122 (T2), and 2MASS 0559–1404 (T5). The most prominent molecular and atomic features are indicated.

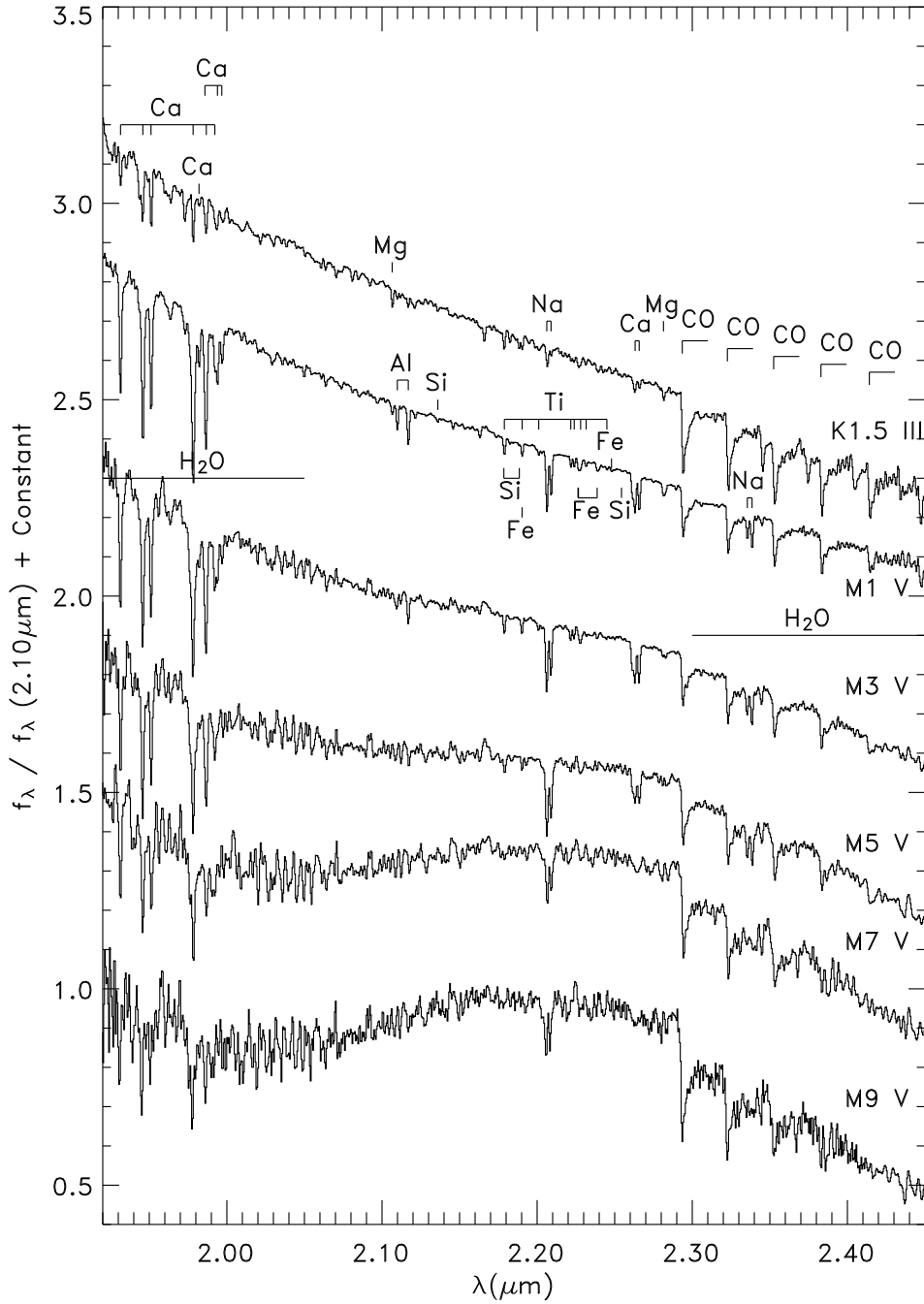


Fig. 12.— *K*-band spectra of Arcturus (K1.5 III), Gl 229A (M1 V), Gl 388 (M3 V), Gl 51 (M5 V) vB 8 (M7 V) and LHS 2924 (M9 V). The most prominent molecular and atomic features are indicated.

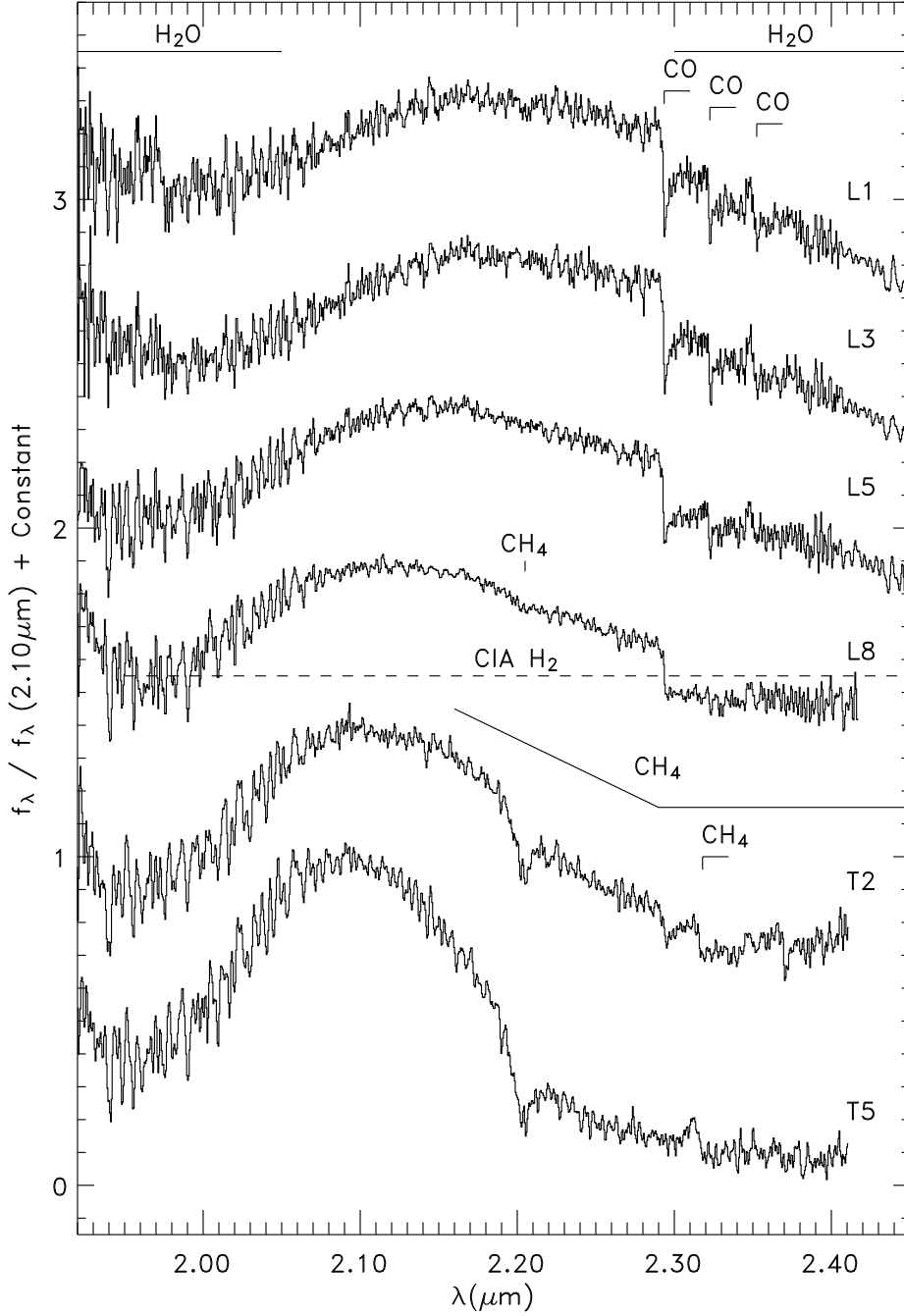


Fig. 13.— *K*-band spectra of 2MASS1439+1929 (L1), 2MASS 1506+1321 (L3), 2MASS 1507–1627 (L5), DENIS 0255–4700 (L8), SDSS 1254–0122 (T2), and 2MASS 0559–1404 (T5). The most prominent molecular and atomic features are indicated.

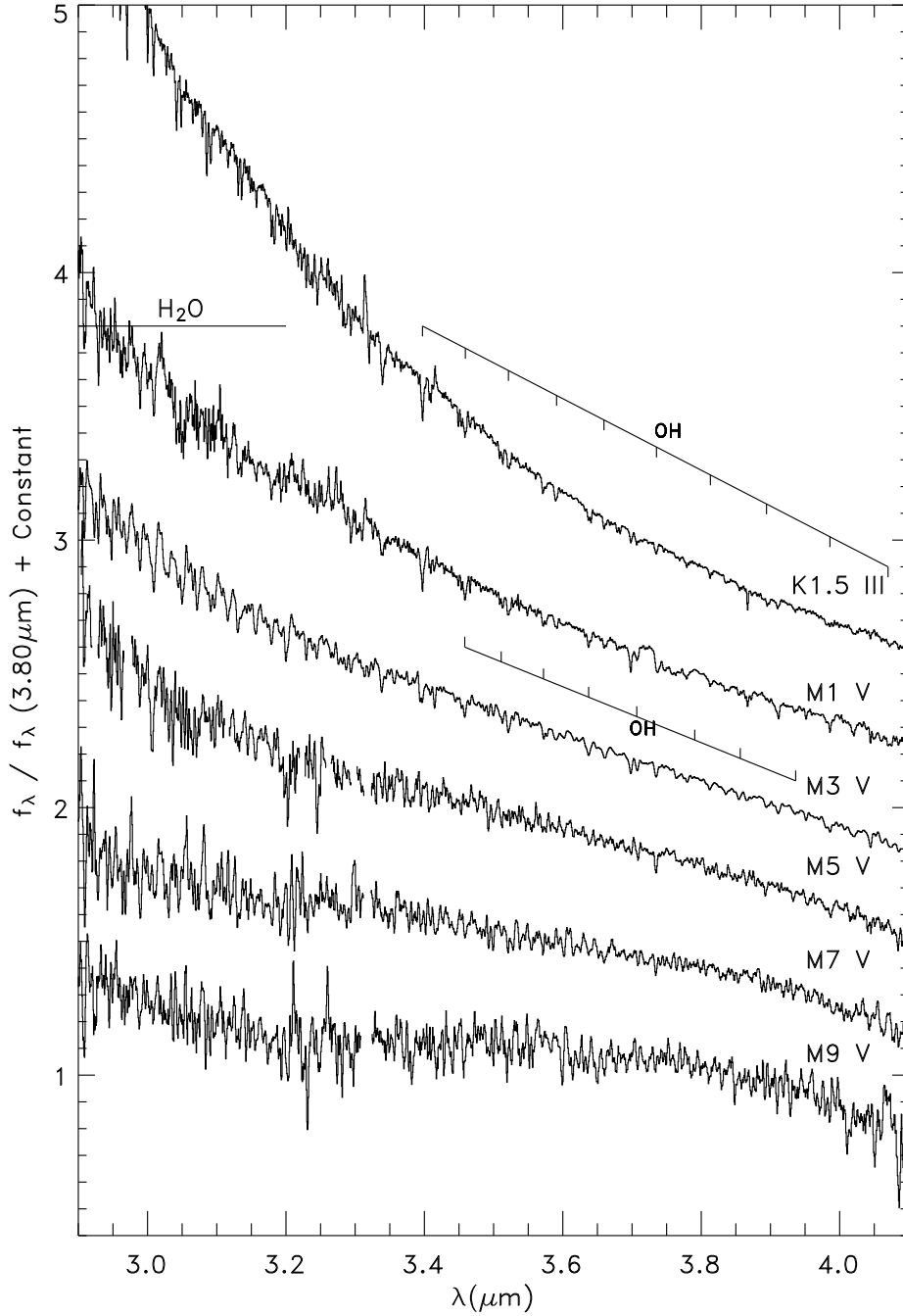


Fig. 14.— *L*-band spectra of Arcturus (K1.5 III), Gl 229A (M1 V), Gl 388 (M3 V), Gl 51 (M5 V) vB 8 (M7 V) and LHS 2924 (M9 V). The most prominent molecular and atomic features are indicated.

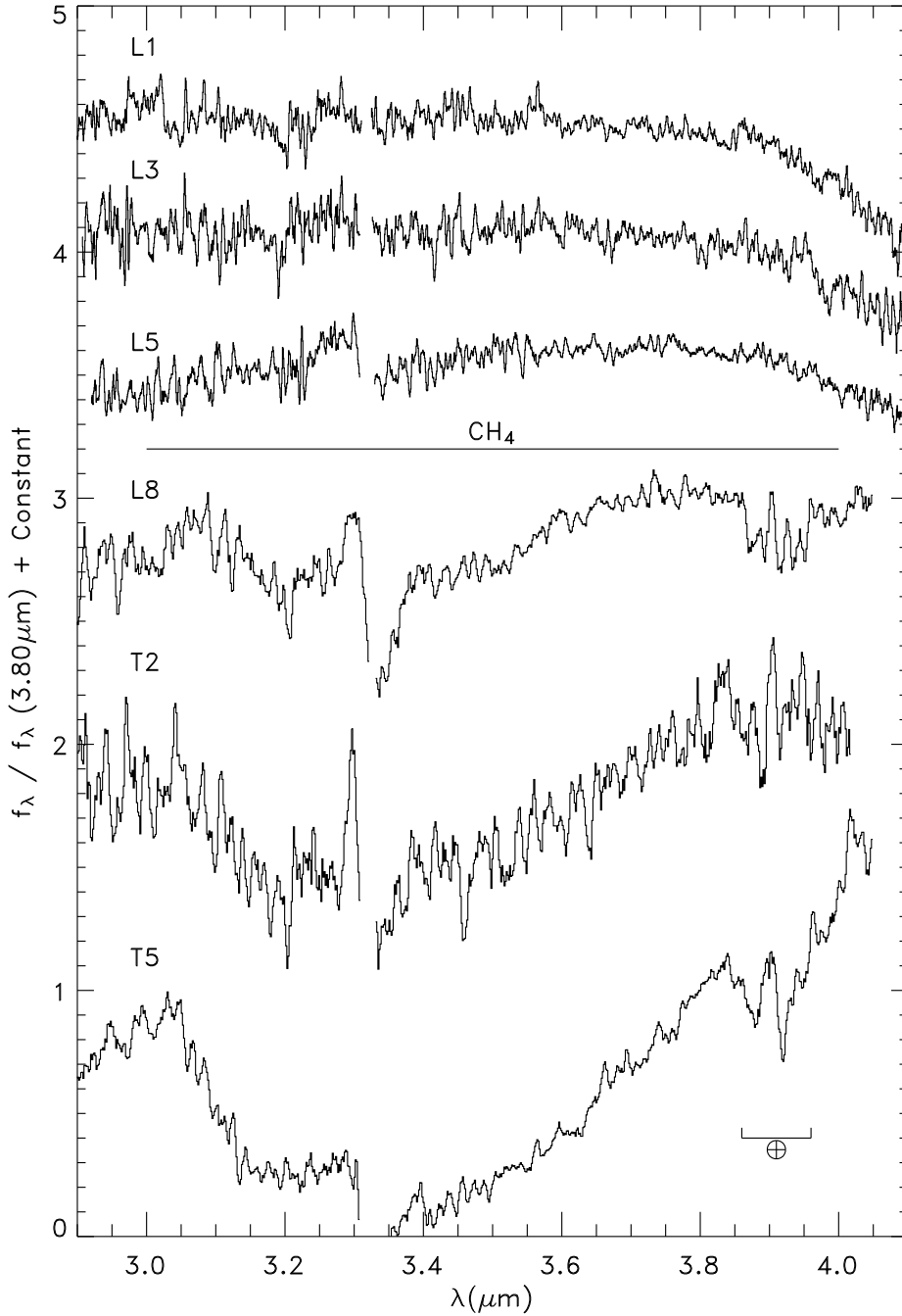


Fig. 15.— *L*-band spectra of 2MASS1439+1929 (L1), 2MASS 1506+1321 (L3), 2MASS 1507–1627 (L5), DENIS 0255–4700 (L8), SDSS 1254–0122 (T2), and 2MASS 0559–1404 (T5). The most prominent molecular and atomic features are indicated. The absorption features seen in the spectra of DENIS 0255–4700 and 2MASS 0559–1404 centered at $\sim 3.9 \mu\text{m}$ are due to incomplete removal of the N_2O telluric feature.

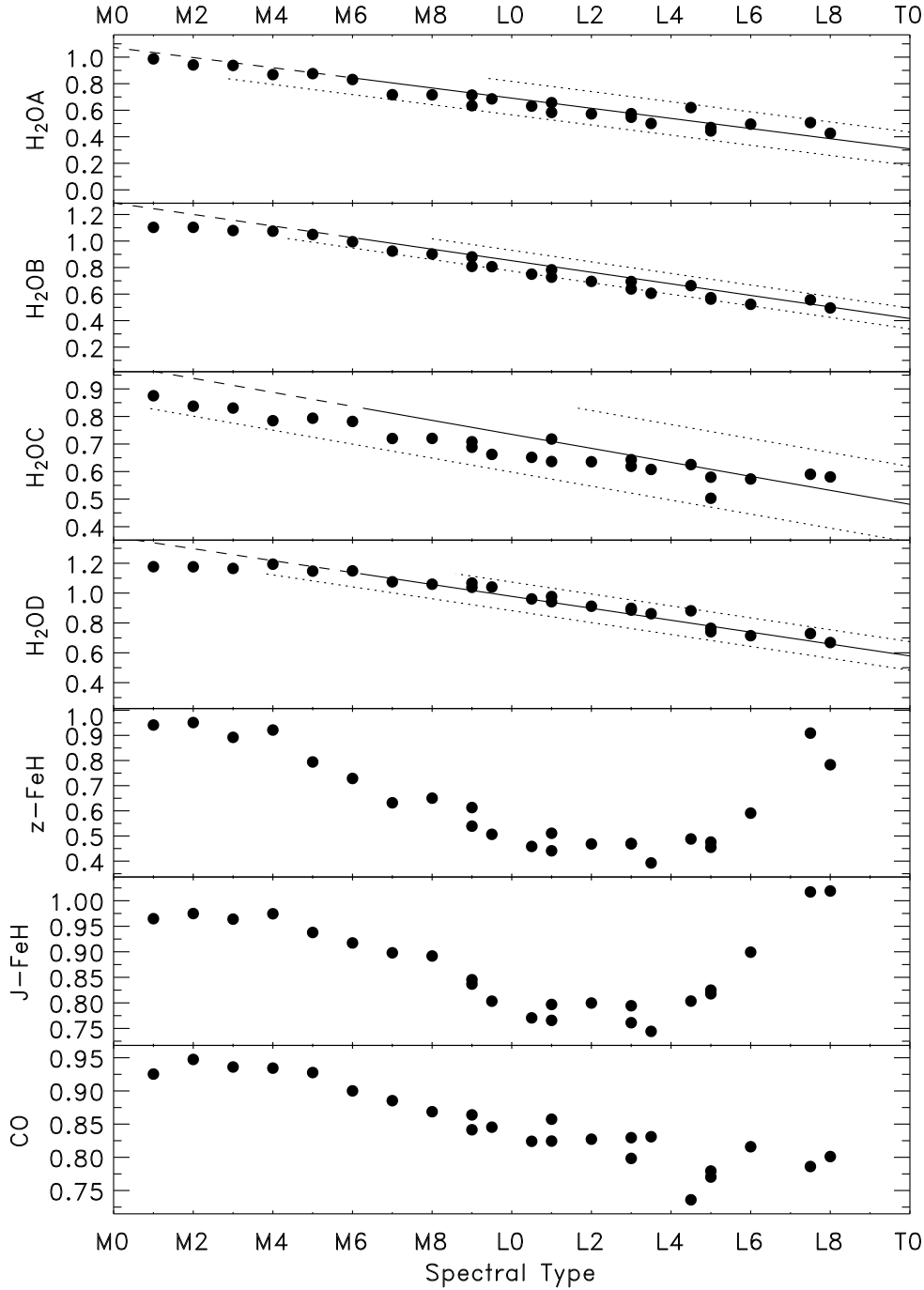


Fig. 16.— The values of the spectral indices of McLean et al. (2003) for the M and L dwarfs in our sample as a function of spectral type. Also shown for the H₂O indices are the best fitting linear relations derived by McLean et al. (2003) from their data. The solid lines show the spectral type range over which the lines were derived (M6 to T8) while the dashed lines show the extension of the solid lines to earlier spectral types. The dotted lines denote the 3σ uncertainties on the relations.

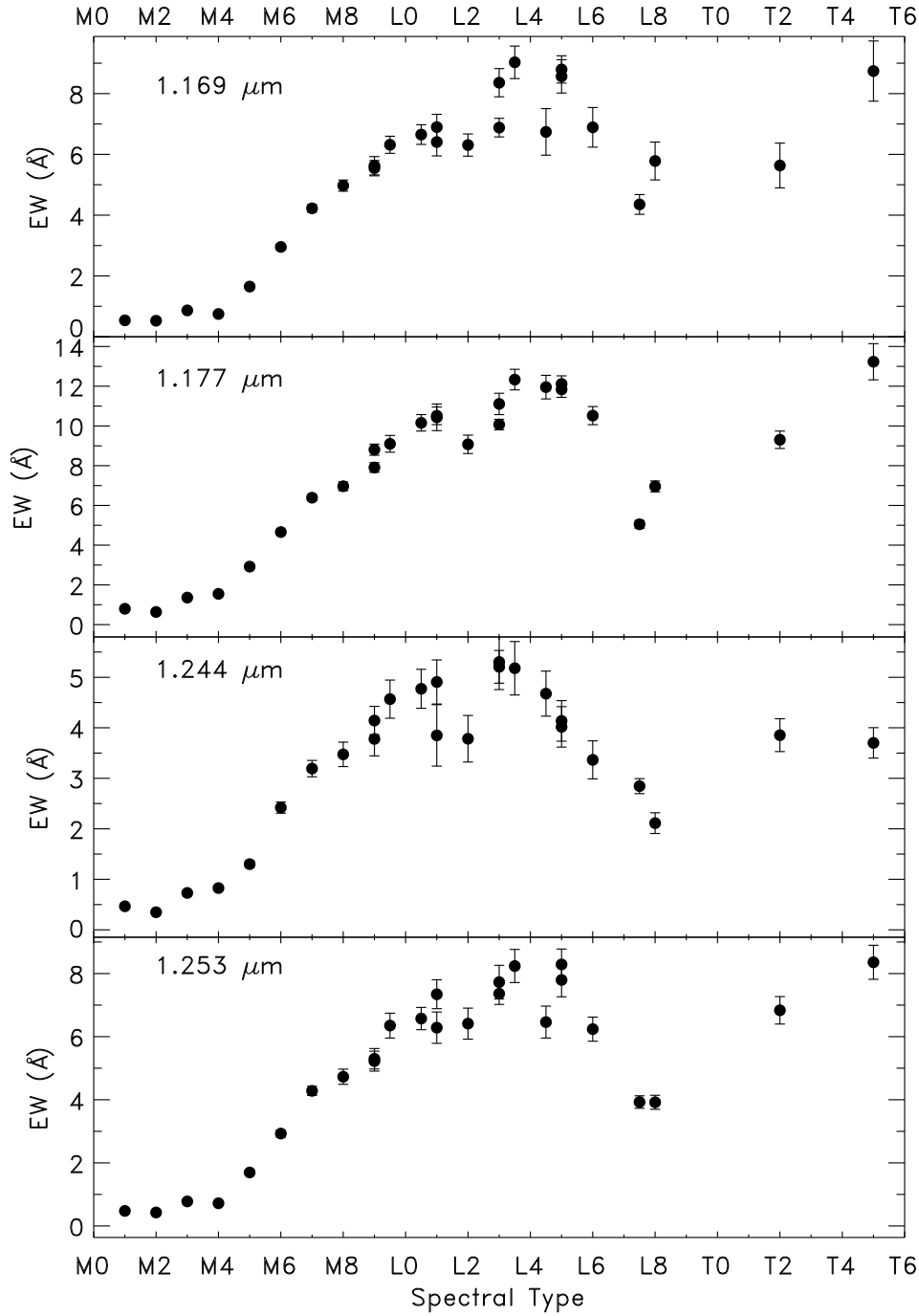


Fig. 17.— The EWs of the K I lines in the spectra of the dwarfs in our sample as a function of spectral type.

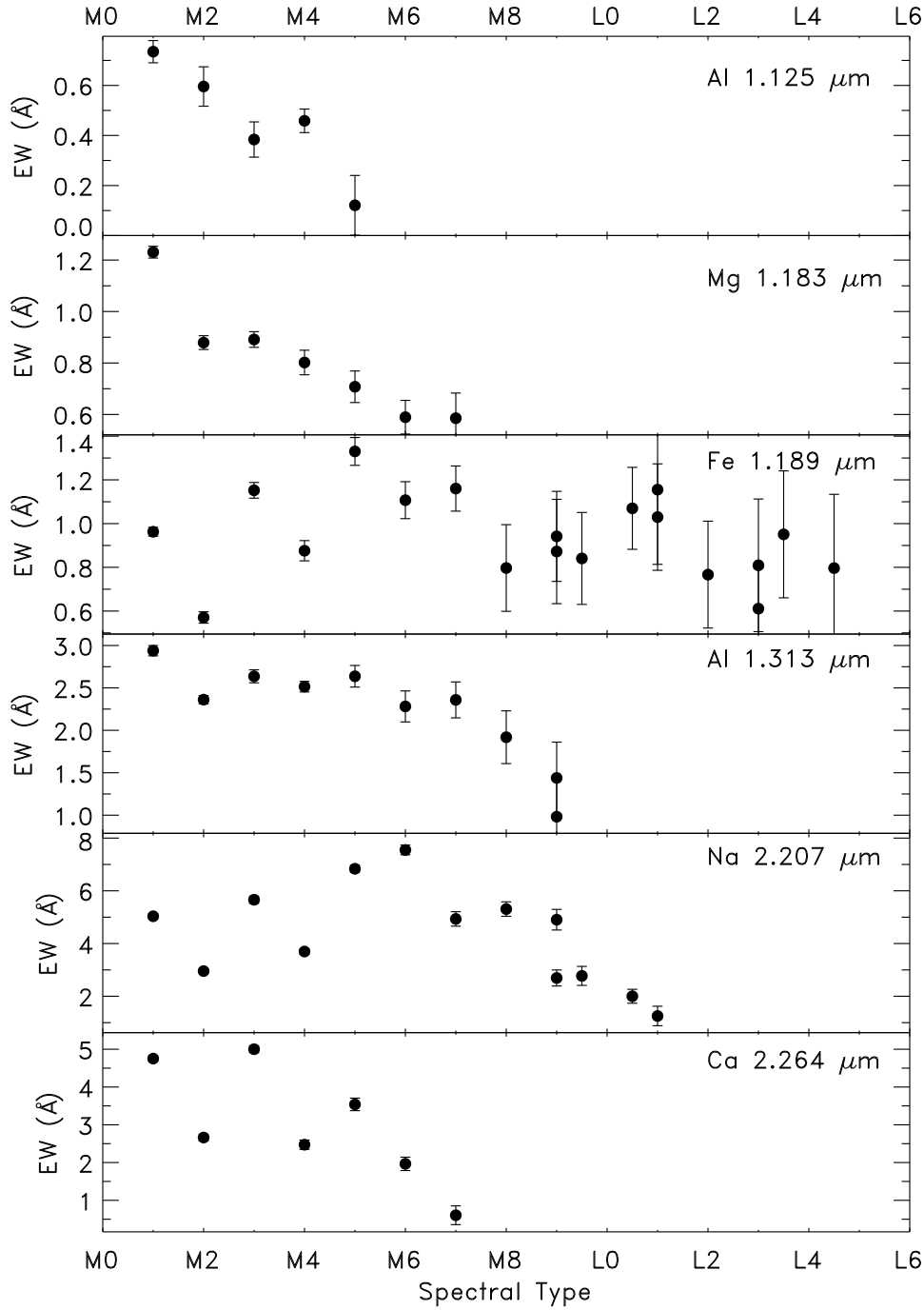


Fig. 18.— The EWs of prominent lines of Al, Fe, Mg, Ca, and Na in the spectra of the dwarfs in our sample as a function of spectral type.

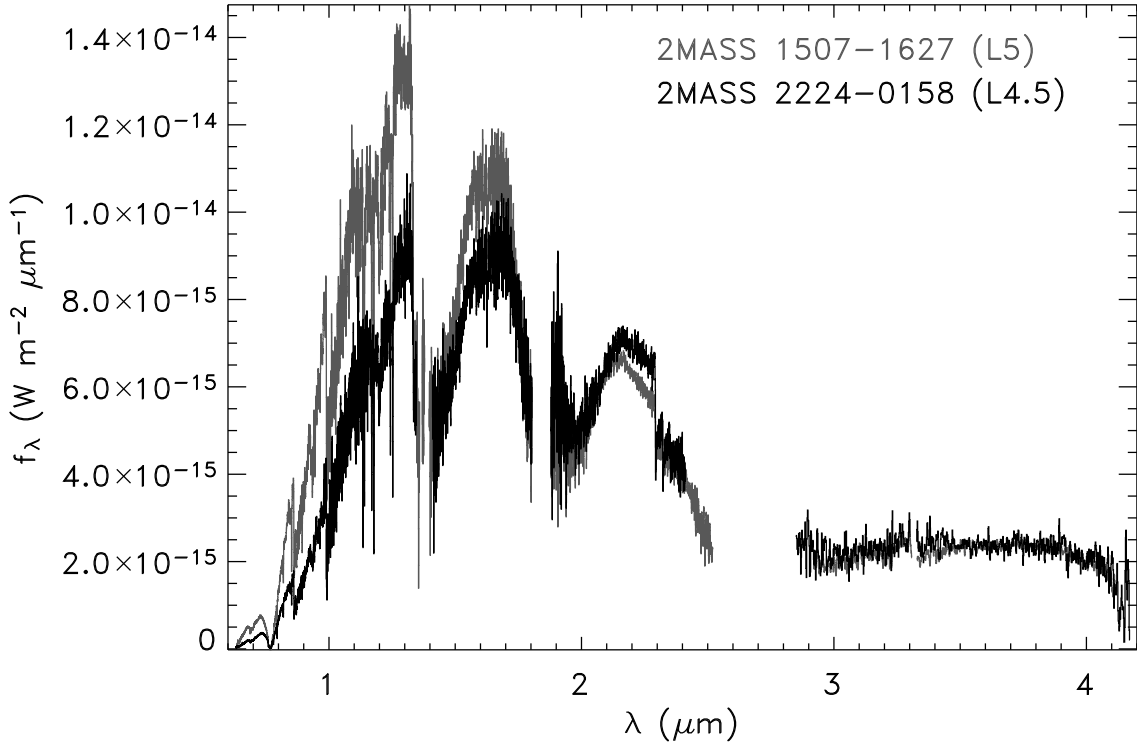


Fig. 19.— 0.6 to 2.4 μm spectra of 2MASS 2224–0158 (L4.5) and 2MASS 1507–1627 (L5). The spectrum of 2MASS 1507–1627 has been scaled to appear as if the object were at the distance of 2MASS 2224–0158. The J - and H -band peaks of 2MASS 2224–0158 are suppressed relative to that of 2MASS 1507–1627 and the ^{12}CO bandhead in the spectrum of 2MASS 2224–0158 is considerably deeper than in the spectrum of 2MASS 1507–1627.

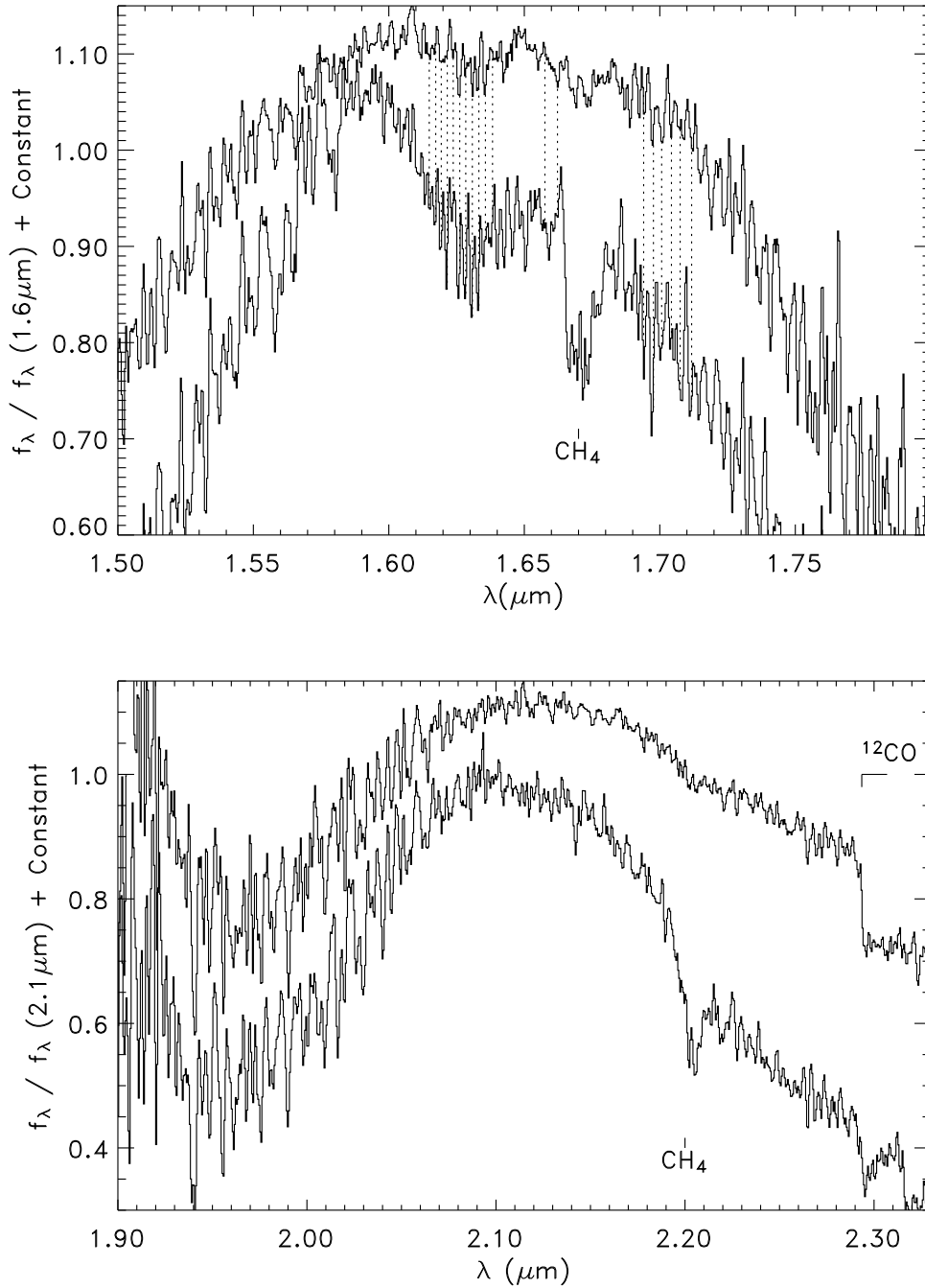


Fig. 20.— The H - (upper panel) and K -band (lower panel) spectra of DENIS 0255–4700 (upper spectrum) and SDSS 1254–0122 (lower spectrum). The CH_4 features identified in the spectrum of the 2MASS 0559–1404 are indicated with dotted lines. Note not all of the CH_4 lines identified in the spectrum of 2MASS 0559–1404 are present in the spectra of DENIS 0255–4700 and SDSS 1254–0122.

Table 1. The Sample

Object	Spectral Type	J (mag)	H (mag)	K (mag)	L' (mag)	π (mas)	π Ref.
(1)	(2)	(3)	(4)	(5)	(6)	(7)	(8)
Gl 229A	M1 V	4.98 ± 0.03	4.35 ± 0.03	4.15 ± 0.03	4.06 ± 0.05	173.19 ± 1.12	1
Gl 411	M2 V	4.10 ± 0.03	3.56 ± 0.03	3.36 ± 0.03	...	392.52 ± 0.91	1
Gl 388	M3 V	5.449 ± 0.027	4.843 ± 0.020	4.593 ± 0.017	...	204.6 ± 2.8	2
Gl 213	M4 V	7.124 ± 0.021	6.627 ± 0.018	6.389 ± 0.016	6.01 ± 0.05	172.75 ± 3.88	1
Gl 51	M5 V	8.611 ± 0.027	8.014 ± 0.023	7.718 ± 0.020	7.35 ± 0.06	95.5 ± 7.3	2
Gl 406	M6 V	7.085 ± 0.024	6.482 ± 0.042	6.084 ± 0.017	5.71 ± 0.05	419.1 ± 2.1	2
vB 8	M7 V	9.776 ± 0.029	9.201 ± 0.024	8.816 ± 0.023	...	154.5 ± 0.7	3
vB 10	M8 V	9.90 ± 0.03	9.24 ± 0.03	8.80 ± 0.03	8.18 ± 0.05	170.25 ± 1.37	1
LP 944–20	M9 V	10.725 ± 0.021	10.017 ± 0.021	9.548 ± 0.023	...	201.4 ± 4.2	5
LHS 2924	M9 V	11.990 ± 0.021	11.225 ± 0.029	10.744 ± 0.024	10.12 ± 0.03	92.4 ± 1.3	2
BRI 0021–0214	M9.5 V	11.992 ± 0.035	11.084 ± 0.022	10.539 ± 0.023	9.78 ± 0.13	86.6 ± 4.0	4
2MASS J07464256+2000321AB	L0.5	11.759 ± 0.020	11.007 ± 0.022	10.468 ± 0.022	9.67 ± 0.03	81.9 ± 0.3	5
2MASS J14392836+1929149	L1	12.759 ± 0.019	12.041 ± 0.019	11.546 ± 0.022	10.80 ± 0.05	69.6 ± 0.5	5
2MASS J02081833+2542533	L1	13.989 ± 0.026	13.107 ± 0.030	12.588 ± 0.027
Kelu-1	L2	13.414 ± 0.026	12.392 ± 0.025	11.747 ± 0.023	10.78 ± 0.15	53.6 ± 2.0	5
2MASS J11463449+2230527AB	L3	14.165 ± 0.028	13.182 ± 0.026	12.590 ± 0.026	...	36.8 ± 0.8	5
2MASS J15065441+1321060	L3	13.365 ± 0.023	12.380 ± 0.021	11.741 ± 0.019
2MASS J00361617+1821104	L3.5	12.466 ± 0.027	11.588 ± 0.029	11.058 ± 0.021	10.08 ± 0.05	114.2 ± 0.8	5
2MASS J22244381–0158521	L4.5	14.073 ± 0.027	12.818 ± 0.026	12.022 ± 0.023	10.90 ± 0.05	88.1 ± 0.1	5
2MASS J15074769–1627386	L5	12.830 ± 0.027	11.895 ± 0.024	11.312 ± 0.026	9.98 ± 0.03	136.4 ± 0.6	5
SDSS J053951.99–005902.0	L5	14.033 ± 0.031	13.104 ± 0.026	12.527 ± 0.024	11.32 ± 0.05	76.12 ± 2.17	6
2MASS 15150083+4847416 ^a	L6 ^a	14.111 ± 0.029	13.099 ± 0.031	12.500 ± 0.024
2MASS J08251968+2115521	L7.5	15.100 ± 0.034	13.792 ± 0.032	13.028 ± 0.026	11.53 ± 0.03	93.8 ± 1.0	5
DENIS-P 025503.3–470049.0	L8	13.246 ± 0.027	12.204 ± 0.024	11.558 ± 0.024
SDSS J125453.90–012247.4	T2	14.891 ± 0.035	14.09 ± 0.025	13.837 ± 0.054	12.25 ± 0.05	84.9 ± 1.9	5
2MASS J05591915–1404489	T5	13.802 ± 0.024	13.679 ± 0.044	13.577 ± 0.052	12.14 ± 0.05	97.7 ± 1.3	5

^a

Infrared spectral type

Note. — J , H , and K -band photometry from the 2MASS Point Source Catalog except for Gl 229A, Gl 411, and vB 10 which are from Leggett (1992) and on the CIT system. L' -band photometry from Leggett et al. (1998), Leggett et al. (2002), Golimowski et al. (2004).

References. — (1) Perryman et al. (1997); (2) van Altena et al. (1995); (3) Monet et al. (1992); (4) Tinney et al. (1995); (5) Dahn et al. (2002); (6) Vrba et al. (2004)

Table 2. Log of SpeX Observations

Object	Spectral Type	UT Date	Spectroscopy Mode	R	Exp. Time (sec)	A0 V Standard
(1)	(2)	(3)	(4)	(5)	(6)	(7)
Gl 229A	M1 V	2002-01-10	SXD	2000	200	HD 42301
		2002-01-11	LXD2.1	2500	250	HD 42301
Gl 411	M2 V	2000-12-10	SXD	2000	60	HD 88960
		2000-12-10	LXD2.3	2500	500	HD 88960
Gl 388	M3 V	2000-12-10	SXD	2000	180	HD 88960
		2000-12-10	LXD2.3	1500	250	HD 88960
Gl 213	M4 V	2000-12-09	SXD	2000	720	HD 34203
		2000-12-09	LXD2.3	2500	500	HD 34203
Gl 51	M5 V	2000-11-06	SXD	2000	600	HD 5071
		2000-11-06	LXD2.3	1500	250	HD 11946
Gl 406	M6 V	2001-01-25	SXD	2000	360	HD 97585
		2001-01-24	LXD2.3	2500	500	HD 97585
vB 8	M7 V	2001-07-12	SXD	2000	1440	HD 148968
		2001-07-12	LXD1.9	938	660	HD 148968
vB 10	M8 V	2001-07-13	SXD	2000	1440	HD 183324
		2001-07-13	LXD1.9	938	600	HD 183324
LP 944–20	M9 V	2001-01-24	SXD	2000	1080	HD 18735
		2002-01-11	LXD1.9	938	2400	HD 183324
LHS 2924	M9 V	2003-02-23	SXD	2000	1200	HD 127304
		2003-02-24	LXD1.9	938	600	HD 127304
BRI 0021–0214	M9.5 V	2001-10-12	SXD	2000	1440	HD 9485
		2000-11-06	LXD1.9	938	720	HD 1663
2MASS 0746+2000AB	L0.5	2001-01-25	SXD	2000	1920	HD 64648
		2002-02-28	LXD1.9	938	1800	HD 64648
2MASS 1439+1929	L1	2001-03-22	SXD	2000	2160	HD 131951
		2003-07-06	LXD1.9	938	2280	HD 131951
2MASS 0208+2542	L1	2002-11-11	SXD	2000	2640	HD 13869
Kelu–1	L2	2001-01-25	SXD	2000	3120	HD 119752
		2001-01-24	LXD1.9	938	2460	HD 119752
		2002-02-28	LXD1.9	938	2280	HD 119752
2MASS 1146+2230AB	L3	2001-03-13	SXD	1200	3360	HD 105388
		2001-03-14	SXD	1200	4800	HD 105388
2MASS 1506+1321	L3	2001-03-13	SXD	2000	2640	HD 131951
		2002-02-28	LXD1.9	938	1800	HD 131951
2MASS 0036+1821	L3.5	2003-08-05	SXD	2000	1200	HD 6457
		2003-08-05	LXD1.9	938	1800	HD 6457
2MASS 2224–0158	L4.5	2001-08-07	SXD	2000	4320	HD 212404
2MASS 1507–1627	L5	2001-03-14	SXD	2000	2160	HD 133772
		2001-03-22	SXD	2000	2400	HD 133772
		2002-02-28	LXD1.9	938	1200	HD 124683
SDSS 0539–0059	L5	2001-01-24	SXD	1200	2400	HD 35656
2MASS 1515+4847	L6	2002-05-28	SXD	2000	4800	HD 116405
2MASS 0825+2115	L7.5	2001-03-12	SXD	1200	6960	HD 64648
		2001-03-13	SXD	1200	2880	HD 64648

Table 2—Continued

Object (1)	Spectral Type (2)	UT Date (3)	Spectroscopy Mode (4)	R (5)	Exp. Time (sec) (6)	A0 V Standard (7)
		2001-03-14	SXD	1200	3120	HD 64648
DENIS 0255–4700	L8	2003-09-21	SXD	2000	1500	HD 21638
SDSS 1254–0122	T2	2001-01-25	SXD	1200	1920	HD 111744
		2001-03-13	SXD	1200	4080	HD 109309
2MASS 0559–1404	T5	2001-01-25	SXD	1200	2880	HD 41695

Table 3. Dwarf Color Residuals

$\langle \delta_{J-H} \rangle$	$\langle \delta_{H-K} \rangle$	$\langle \delta_{K-L'} \rangle$
$+0.00 \pm 0.04$	$+0.02 \pm 0.03$	-0.01 ± 0.07

Note. — $\delta_{X-Y} = (X - Y)_{\text{obs}} - (X - Y)_{\text{synt}}$.
The errors are given by the RMS deviation.

Table 4. Log of IRCS Observations

Object	Spectral Type	UT Date	R	Exp. Time (sec)	A0 V Standard
(1)	(2)	(3)	(4)	(5)	(6)
2MASS 2224–0158	L4.5	2002-12-12	425	560	HD 215143
SDSS 0539–0059	L5	2002-12-09	425	600	HD 37887
2MASS 0825+2115	L7.5	2001-05-06	212	1800	HD 64648
DENIS0255–4700	L8	2002-12-09	212	252	HD 28813
SDSS 1254–0122	T2	2001-05-06	212	1800	HD 109309
2MASS 0559–1404	T5	2002-12-09	212	2590	HD 47596

Table 5. Molecular Features In Dwarf Spectra

Wavelength (μm) (1)	Species (2)	Transition (3)	Ref. (4)
0.89–0.99	H ₂ O	$3\nu_3, \nu_1 + 2\nu_3, 2\nu_1 + \nu_3, 3\nu_1, \nu_1 + 2\nu_2 + \nu_3, 2\nu_1 + 2\nu_2$	1
0.9896 head	FeH	0–0 band of $F^4\Delta - X^4\Delta$	3
1.00606 Q-branch	FeH	0–0 band of $F^4\Delta - X^4\Delta$	6
1.05–1.08	VO	0–0 band of $A^4\Pi - X^4\Sigma^-$	5
1.09–1.20	H ₂ O	$\nu_2 + 2\nu_3, \nu_1 + \nu_2 + \nu_3, 2\nu_1 + \nu_2, 3\nu_2 + \nu_3, \nu_1 + 2\nu_2$	1
1.1–1.24	CH ₄	$3\nu_3$	9
1.1939 head	FeH	0–1 band of $F^4\Delta - X^4\Delta$	3
1.22210 Q-branch	FeH	0–0 band of $F^4\Delta - X^4\Delta$	6
1.2389 head	FeH	1–2 band of $F^4\Delta - X^4\Delta$	3
1.3–1.51	H ₂ O	$2\nu_3, \nu_1 + \nu_2, 2\nu_1, 2\nu_2 + \nu_3, \nu_1 + 2\nu_2$	1
1.58263 head	FeH	0–0 band of $E^4\Pi - A^4\Pi$	4
1.59188 head	FeH	0–0 band of $E^4\Pi - A^4\Pi$	4
1.62457 head	FeH	0–0 band of $E^4\Pi - A^4\Pi$	4
1.6–1.8	CH ₄	$2\nu_3, 2\nu_2 + \nu_3$	8
1.75–2.05	H ₂ O	$\nu_2 + \nu_3, \nu_1 + \nu_2, 3\nu_2$	1
2.3–3.2	H ₂ O	$\nu_1, \nu_3, 2\nu_2$	1
2.15–2.5	CH ₄	$\nu_3 + \nu_4, \nu_2 + \nu_3$	8
2.29352 head	¹² CO	2–0 band of $X^1\Sigma^+ - X^1\Sigma^+$	2
2.32266 head	¹² CO	3–1 band of $X^1\Sigma^+ - X^1\Sigma^+$	2
2.34483 head	¹³ CO	2–0 band of $X^1\Sigma^+ - X^1\Sigma^+$	2
2.35246 head	¹² CO	4–2 band of $X^1\Sigma^+ - X^1\Sigma^+$	2
2.38295 head	¹² CO	5–3 band of $X^1\Sigma^+ - X^1\Sigma^+$	2
2.41414 head	¹² CO	6–4 band of $X^1\Sigma^+ - X^1\Sigma^+$	2
1.8–2.8	H ₂	CIA	11
3.4–4.2 heads	OH	$\Delta\nu = +1, +2$ bandheads	10
3.0–3.8	CH ₄	ν_3	7

References. — (1) Auman (1967); (2) Goorvitch (1994); (3) Phillips et al. (1987); (4) Wallace & Hinkle (2001); (5) Chueng et al. (1982); (6) Cushing et al. (2003); (7) Noll et al. (2000); (8) Leggett et al. (2000); (9) Danielson (1966); 10 Wallace & Hinkle (2002); (11) Borysow et al. (1997)

Table 6. Atomic Features in Dwarf Spectra

Vacuum λ (μm)	Elements	Vacuum λ (μm)	Elements	Vacuum λ (μm)	Elements	Vacuum λ (μm)	Elements
0.95500460	Ti I	1.0608472	Si I, Ti I	1.2528860	K I	1.9781980	Ca I
0.96042912	Ti I	1.0664966	Ti I, Si I	1.2682125	Na I	1.9817054	Ca I
0.96408301	Ti I	1.0697268	Si I	1.2827300	H I, Ti I	1.9865941	Ca I
0.96516997	Ti I	1.1258730	Al I	1.2851494	Ti I	1.9930196	Ca I
0.96774343	Ti I	1.1383850	Na I	1.2883723	Fe I	1.9968176	Ca I
0.96923371	Ti I	1.1408517	Na I	1.2904632	Mn I	2.1066365	Mg I
0.97085682	Ti I	1.1593413	Fe I	1.2982085	Mn I	2.1098654	Al I
0.97315592	Ti I	1.1612996	Fe I	1.3130514	Al I	2.1168456	Al I, Si I
0.97465017	Ti I	1.1640519	Fe I	1.4878380	Mg I	2.1789074	Si I, Ti I
0.97708032	Ti I	1.1692427	K I, Fe I	1.5028185	Mg I	2.2062996	Na I
0.97884568	Ti I	1.1778406	K I	1.5046375	Mg I	2.2089866	Na I
0.98357543	Ti I	1.1801096	Fe I	1.5167645	K I	2.2215927	Ti I
1.0219217	Fe I	1.1833522	Mg I	1.5753070	Mg I	2.2237389	Ti I
1.0328393	Sr II	1.1891897	Fe I	1.5771145	Mg I	2.2275054	Fe I, Ti I
1.0347329	Fe I, Ca I	1.1974243	Fe I, Ti I	1.5894133	Si I	2.2317958	Ti I
1.0382309	Si I	1.1995492	Si I	1.6723852	Al I	2.2390381	Fe I
1.0399835	Fe I, Ti I	1.2035899	Si I	1.6755865	Al I	2.2626701	Ca I
1.0426753	Fe I	1.2086007	Mg I	1.7110102	Mg I	2.2656055	Ca I
1.0471180	Fe I	1.2111957	Si I	1.9314969	Ca I	2.2819887	Mg I
1.0500833	Ti I	1.2273618	Si I	1.9458160	Ca I	2.3354050	Na I
1.0588292	Ti I, Si I	1.2436839	K I	1.9509361	Ca I	2.3383542	Na I

Table 7. CH₄ features in Dwarf Spectra

Vacuum Wavelength (μm)	Vacuum Wavelength (μm)
1.6149080	1.6382678
1.6173155	1.6575994
1.6193378	1.6622256
1.6215579	1.6940340
1.6237635	1.6976493
1.6261759	1.7006882
1.6283867	1.7042962
1.6308079	1.7075190
1.6332215	1.7117420
1.6356431	...

Table 8. K I Equivalent Widths

Object	Spectral Type	EW (Å)			
		1.169 μm	1.177 μm	1.244 μm	1.253 μm
(1)	(2)	(3)	(4)	(5)	(6)
Gl 229A	M1 V	0.5 \pm 0.1	0.8 \pm 0.1	0.5 \pm 0.1	0.5 \pm 0.1
Gl 411	M2 V	0.5 \pm 0.1	0.6 \pm 0.1	0.3 \pm 0.1	0.4 \pm 0.1
Gl 388	M3 V	0.9 \pm 0.1	1.4 \pm 0.1	0.7 \pm 0.1	0.8 \pm 0.1
Gl 213	M4 V	0.7 \pm 0.1	1.5 \pm 0.1	0.8 \pm 0.1	0.7 \pm 0.1
Gl 51	M5 V	1.7 \pm 0.1	2.9 \pm 0.1	1.3 \pm 0.1	1.7 \pm 0.1
Gl 406	M6 V	3.0 \pm 0.1	4.7 \pm 0.1	2.4 \pm 0.1	2.9 \pm 0.1
vB 8	M7 V	4.2 \pm 0.1	6.4 \pm 0.2	3.2 \pm 0.2	4.3 \pm 0.1
vB 10	M8 V	5.0 \pm 0.2	7.0 \pm 0.2	3.5 \pm 0.2	4.7 \pm 0.2
LP 944–20	M9 V	5.5 \pm 0.3	7.9 \pm 0.2	3.8 \pm 0.3	5.2 \pm 0.3
LHS 2924	M9 V	5.6 \pm 0.3	8.8 \pm 0.3	4.1 \pm 0.3	5.3 \pm 0.3
BRI 0021–0214	M9.5 V	6.3 \pm 0.3	9.1 \pm 0.4	4.6 \pm 0.4	6.4 \pm 0.4
2MASS 0746+2000AB	L0.5	6.7 \pm 0.3	10.2 \pm 0.4	4.8 \pm 0.4	6.6 \pm 0.4
2MASS 1439+1929	L1	6.9 \pm 0.4	10.5 \pm 0.4	4.9 \pm 0.4	7.3 \pm 0.5
2MASS 0208+2542	L1	6.4 \pm 0.5	10.4 \pm 0.7	3.8 \pm 0.6	6.3 \pm 0.5
Kelu–1	L2	6.3 \pm 0.4	9.1 \pm 0.5	3.8 \pm 0.5	6.4 \pm 0.5
2MASS 1146+2230AB	L3	6.9 \pm 0.3	10.1 \pm 0.3	5.2 \pm 0.3	7.4 \pm 0.3
2MASS 1506+1321	L3	8.4 \pm 0.5	11.1 \pm 0.5	5.3 \pm 0.5	7.7 \pm 0.5
2MASS 0036+1821	L3.5	9.0 \pm 0.5	12.3 \pm 0.5	5.2 \pm 0.5	8.2 \pm 0.5
2MASS 2224–0158	L4.5	6.7 \pm 0.8	12.0 \pm 0.6	4.7 \pm 0.4	6.5 \pm 0.5
2MASS 1507–1627	L5	8.6 \pm 0.5	11.8 \pm 0.4	4.1 \pm 0.4	7.8 \pm 0.5
SDSS 0539–0059	L5	8.8 \pm 0.4	12.1 \pm 0.4	4.0 \pm 0.4	8.3 \pm 0.5
2MASS 1515+4847	L6	6.9 \pm 0.7	10.5 \pm 0.5	3.4 \pm 0.4	6.2 \pm 0.4
2MASS 0825+2115	L7.5	4.4 \pm 0.3	5.1 \pm 0.2	2.8 \pm 0.1	3.9 \pm 0.2
DENIS 0255–4700	L8	5.8 \pm 0.6	7.0 \pm 0.3	2.1 \pm 0.2	3.9 \pm 0.2
SDSS 1254–0122	T2	5.6 \pm 0.7	9.3 \pm 0.4	3.9 \pm 0.3	6.8 \pm 0.4
2MASS 0559–1404	T5	8.7 \pm 1.0	13.2 \pm 0.9	3.7 \pm 0.3	8.4 \pm 0.5

Table 9. Equivalent Widths of Other Lines

Object	Spectral Type	EW (Å)					
		Al I	Mg I	Fe I	Al I	Na I	Ca I
		1.125 μm	1.183 μm	1.189 μm	1.132 μm	2.207 μm	2.264 μm
(1)	(2)	(3)	(4)	(5)	(6)	(7)	(8)
GI 229A	M1 V	0.7 \pm 0.1	1.2 \pm 0.1	1.0 \pm 0.1	2.9 \pm 0.1	5.0 \pm 0.1	4.7 \pm 0.1
GI 411	M2 V	0.6 \pm 0.1	0.9 \pm 0.1	0.6 \pm 0.1	2.4 \pm 0.1	3.0 \pm 0.1	2.7 \pm 0.1
GI 388	M3 V	0.4 \pm 0.1	0.9 \pm 0.1	1.2 \pm 0.1	2.6 \pm 0.1	5.7 \pm 0.1	5.0 \pm 0.1
GI 213	M4 V	0.5 \pm 0.1	0.8 \pm 0.1	0.9 \pm 0.1	2.5 \pm 0.1	3.7 \pm 0.1	2.5 \pm 0.1
GI 51	M5 V	0.1 \pm 0.1	0.7 \pm 0.1	1.3 \pm 0.1	2.6 \pm 0.1	6.8 \pm 0.1	3.5 \pm 0.2
GI 406	M6 V	...	0.6 \pm 0.1	1.1 \pm 0.1	2.3 \pm 0.2	7.6 \pm 0.2	2.0 \pm 0.2
vB 8	M7 V	...	0.6 \pm 0.1	1.2 \pm 0.1	2.4 \pm 0.2	4.9 \pm 0.3	0.6 \pm 0.2
vB 10	M8 V	0.8 \pm 0.2	2.0 \pm 0.3	5.3 \pm 0.3	...
LP 944–20	M9 V	0.9 \pm 0.2	1.0 \pm 0.4	2.7 \pm 0.3	...
LHS 2924	M9 V	0.9 \pm 0.2	1.4 \pm 0.4	4.9 \pm 0.4	...
BRI 0021–0214	M9.5 V	0.8 \pm 0.2	...	2.8 \pm 0.4	...
2MASS 0746+2000AB	L0.5	1.1 \pm 0.2	...	2.0 \pm 0.3	...
2MASS 1439+1929	L1	1.0 \pm 0.2	...	1.3 \pm 0.4	...
2MASS 0208+2542	L1	1.2 \pm 0.3
Kelu–1	L2	0.8 \pm 0.2
2MASS 1146+2230AB	L3	0.6 \pm 0.2
2MASS 1506+1321	L3	0.8 \pm 0.3
2MASS 0036+1821	L3.5	1.0 \pm 0.3
2MASS 2224–0158	L4.5	0.8 \pm 0.3

Table 10. f_{bol} and L_{bol} of the Dwarfs

Object	Spectral Type	f_{bol} (W m^{-2})	$m_{\text{bol}}^{\text{a}}$	$\log_{10}(L_{\text{bol}}/L_{\odot})^{\text{b}}$	M_{bol}
(1)	(2)	(3)	(4)	(5)	(6)
Gl 229A	M1 V	$5.19\text{E}-11 \pm 1.43\text{E}-12$	6.72 ± 0.03	-1.27 ± 0.01	7.92 ± 0.03
Gl 411	M2 V	$1.10\text{E}-10 \pm 3.03\text{E}-12$	5.91 ± 0.03	-1.66 ± 0.01	8.88 ± 0.03
Gl 388	M3 V	$3.24\text{E}-11 \pm 7.11\text{E}-13$	7.24 ± 0.03	-1.62 ± 0.02	8.79 ± 0.04
Gl 213	M4 V	$5.97\text{E}-12 \pm 1.24\text{E}-13$	9.07 ± 0.02	-2.21 ± 0.02	10.26 ± 0.05
Gl 51	M5 V	$1.49\text{E}-12 \pm 3.49\text{E}-14$	10.58 ± 0.03	-2.30 ± 0.07	10.48 ± 0.17
Gl 406	M6 V	$5.90\text{E}-12 \pm 1.40\text{E}-13$	9.08 ± 0.03	-2.98 ± 0.01	12.20 ± 0.03
vB 8	M7 V	$4.73\text{E}-13 \pm 1.18\text{E}-14$	11.83 ± 0.03	-3.21 ± 0.01	12.77 ± 0.03
vB 10	M8 V	$4.28\text{E}-13 \pm 1.19\text{E}-14$	11.93 ± 0.03	-3.34 ± 0.01	13.09 ± 0.03
LP 944–20	M9 V	$2.02\text{E}-13 \pm 4.67\text{E}-15$	12.75 ± 0.03	-3.81 ± 0.02	14.27 ± 0.05
LHS 2924	M9 V	$6.57\text{E}-14 \pm 1.62\text{E}-15$	13.97 ± 0.03	-3.62 ± 0.02	13.79 ± 0.04
BRI 0021–0214	M9.5 V	$7.43\text{E}-14 \pm 1.88\text{E}-15$	13.84 ± 0.03	-3.51 ± 0.04	13.52 ± 0.10
2MASS 0746+2000AB	L0.5	$8.07\text{E}-14 \pm 2.09\text{E}-15$	13.75 ± 0.03	-3.43 ± 0.01	13.31 ± 0.03
2MASS 1439+1929	L1	$3.00\text{E}-14 \pm 7.31\text{E}-16$	14.82 ± 0.03	-3.72 ± 0.01	14.03 ± 0.03
Kelu–1	L2	$2.02\text{E}-14 \pm 5.09\text{E}-16$	15.25 ± 0.03	-3.66 ± 0.03	13.89 ± 0.09
2MASS 1506+1321	L3	$2.21\text{E}-14 \pm 5.74\text{E}-16$	15.15 ± 0.03
2MASS 0036+1821	L3.5	$4.55\text{E}-14 \pm 1.35\text{E}-15$	14.37 ± 0.03	-3.97 ± 0.01	14.65 ± 0.04
2MASS 2224–0158	L4.5	$1.58\text{E}-14 \pm 4.84\text{E}-16$	15.51 ± 0.03	-4.20 ± 0.01	15.24 ± 0.03
2MASS 1507–1627	L5	$3.54\text{E}-14 \pm 1.08\text{E}-15$	14.64 ± 0.03	-4.16 ± 0.01	15.15 ± 0.03
SDSS 0539–0559	L5	$1.20\text{E}-14 \pm 3.79\text{E}-16$	15.81 ± 0.03	-4.19 ± 0.03	15.22 ± 0.07
2MASS 0825+2115	L7	$7.51\text{E}-15 \pm 3.51\text{E}-16$	16.32 ± 0.05	-4.58 ± 0.02	16.18 ± 0.05
DENIS 0255–4700	L8	$3.15\text{E}-14 \pm 1.46\text{E}-15$	14.76 ± 0.05
SDSS 1254–0122	T2	$4.82\text{E}-15 \pm 3.30\text{E}-16$	16.81 ± 0.07	-4.68 ± 0.04	16.45 ± 0.09
2MASS 0559–1404	T5	$8.55\text{E}-15 \pm 6.22\text{E}-16$	16.18 ± 0.08	-4.56 ± 0.03	16.13 ± 0.08

^a

$$m_{\text{bol}} = -2.5 \times \log(f_{\text{bol}}) - 18.988 \text{ assuming } L_{\odot} = 3.86 \times 10^{26} \text{ W and } M_{\text{bol}\odot} = +4.74.$$

$$^{\text{b}}\log(L_{\text{bol}}/L_{\odot}) = \log(f_{\text{bol}}) - 2 \times \log(\pi) + 7.4913 \text{ assuming } L_{\odot} = 3.86 \times 10^{26} \text{ W}.$$